Progress in Oceanography 229 (2024) 103367

Contents lists available at ScienceDirect

Progress in Oceanography

journal homepage: www.elsevier.com/locate/pocean

# Changes in glacial meltwater system around Amundsen sea Polynya illustrated by radium and oxygen isotopes

Guanghui Chen [a], You Jiang [a], Yi Wang [a], Jun Zhao [b], Yusheng Qiu [a], Minfang Zheng [a], Mengya Chen [a], Jianming Pan [b], Min Chen [a,*]

[a] College of Ocean and Earth Sciences, Xiamen University, Xiamen 361102, China
[b] Key Laboratory of Marine Ecosystem Dynamics, Second Institute of Oceanography, Ministry of Natural Resources, Hangzhou 310012, China

ARTICLE INFO

*Keywords:*
Glacial meltwater
Brine
Oxygen isotope
Radium
Amundsen Sea Polynya

ABSTRACT

The Amundsen Sea Polynya (ASP) is the most biologically productive area around Antarctica due to the input of iron-rich glacial meltwater (GMW). However, the source and path of GMW in the ASP, and how these have changed since the Dotson Ice Shelf (DIS), a primary GMW supplier, began experiencing a cooling period after 2011, remain unclear. This study presents the distribution of GMW in the ASP during the austral summer of 2020. Subsurface GMW proportions were estimated using a composite tracer derived from potential temperature, salinity, and dissolved oxygen, while surface GMW were using $^{226}$Ra and $^{228}$Ra. The results indicate that GMW in the ASP originates from DIS and Pine Island Bay. Surface GMW upwelled from the melting basal cavity of DIS is transported northwestward by katabatic winds, while subsurface GMW is transported northwestward beneath the mixed layer, with the upper portion upwelling to the surface in the ASP center along isopycnals ($\sigma_\theta$) of 27.40 to 27.45 kg/m$^3$. Depth variations of these isopycnals correlate well with brine inventories released by winter sea ice formation, suggesting that sea ice formation influences seawater $\sigma_\theta$ structures and consequently the transport path of subsurface GMW. Compared to 2011, the GMW content in the ASP in 2020 decreased by nearly half, and the transport routes have also changed. These changes align with the significantly reduced GMW discharge from the DIS after 2012. Our study confirms that the GMW system in the ASP has undergone significant changes following the onset of the cooling period experienced by the DIS.

## 1. Introduction

In the context of climate change, the Southern Ocean is experiencing rapid warming (Gille, 2008; Dutrieux et al., 2014; Schmidtko et al., 2014; Gao et al., 2018). This warming intensifies the upwelling of warm Circumpolar Deep Water (CDW) onto the continental shelves, subsequently accelerating the basal melting of ice shelves (Jacobs et al., 2011; Dinniman et al., 2012; Assmann et al., 2013). In the Amundsen Sea, upwelled CDW enters the continental shelf and approaches the bases of ice shelves through glacial troughs (Walker et al., 2007; Wåhlin et al., 2010; Jacobs et al., 2011, 2012; Arneborg et al., 2012; Biddle et al., 2017, 2019), causing the coastal ice shelves to experience the most intense basal melting around Antarctica (Rignot et al., 2002, 2013; Pritchard et al., 2012; Paolo et al., 2015).

Primary productivity in the Southern Ocean is thought to be limited by bioavailable iron, except in coastal polynyas adjacent to ice shelves, where iron-rich meltwater discharges fuel phytoplankton booms (Boyd et al., 2007; Alderkamp et al., 2012, 2015; Gerringa et al., 2012; Yager et al., 2012; Arrigo et al., 2015; Sherrell et al., 2015; St-Laurent et al., 2017). Among Antarctic coastal polynyas, the Amundsen Sea Polynya (ASP) is known for the highest biological productivity per unit area (Arrigo and van Dijken, 2003; Arrigo et al., 2015), largely due to GMW input from coastal ice shelves (Alderkamp et al., 2012; Arrigo et al., 2015). The ASP is close to the Dotson Ice Shelf (DIS) and the Getz Ice Shelf (GIS), with thinning rates of 7.8 ± 0.6 and 4.3 ± 0.4 m/yr, respectively (Rignot et al., 2013). Previous studies have suggested that GIS is not the main source of GMW for the ASP (Alderkamp et al., 2015; Randall-Goodwin et al., 2015; Sherrell et al., 2015). In contrast to the ASP, the Pine Island Polynya (PIP) in Pine Island Bay receives more GMW through the Pine Island Ice Shelf (PIIS, thinning rate: 16.2 ± 1.0 m/yr) and the Thwaites Ice Shelf (TIS, thinning rate: 17.7 ± 1.0 m/yr) (Rignot et al., 2013). However, the average primary production in the PIP (566.1 ± 198.9 mg C m$^{-2}$ d$^{-1}$) is lower than in the ASP (802.9 ± 165.7 mg C m$^{-2}$ d$^{-1}$) (Arrigo et al., 2015). To account for this

* Corresponding author.
*E-mail address:* mchen@xmu.edu.cn (M. Chen).

https://doi.org/10.1016/j.pocean.2024.103367
Received 12 July 2022; Received in revised form 1 July 2024; Accepted 18 October 2024
Available online 24 October 2024

inconsistency, Arrigo et al. (2015) assessed that the main suppliers of bioavailable iron in the ASP were DIS, TIS, and Crosson Ice Shelf (CIS). Therefore, the source of GMW-iron supporting phytoplankton growth in the ASP remains unclear.

Previous studies have shown that GMW inputs suppress the formation of Antarctic Bottom Water (AABW) by counteracting the increase in the salinity of shelf waters (Williams et al., 2016; Silvano et al., 2018). As one of the main sources of AABW, the salinity of dense shelf water (DSW) in the Ross Sea decreased by 0.03 psu per decade (Jacobs and Giulivi, 2010). From 1958 to 2008, the salinity of the westward coastal currents from the Amundsen Sea decreased at a rate of 0.08 psu per decade, during which glaciers in the Amundsen Sea retreated rapidly under accelerated basal melting (Jacobs and Giulivi, 2010; Pritchard et al., 2012; Paolo et al., 2015; Jenkins et al., 2018; Jacobs et al., 2022). However, recent studies have confirmed a sharp recovery in DSW salinity in the Ross Sea since 2013 (Castagno et al., 2019; Guo et al., 2021), consistent with a pause in the accelerated mass loss from the Amundsen Sea glaciers since 2011 (The IMBIE team, 2018). The DIS, one of the coastal ice shelves in the Amundsen Sea embayment, has experienced a cool period since 2012, with a rapid decline in meltwater discharge flux from 88.2 ± 23.4 Gt/yr in 2009 to 20.9 ± 3.3 Gt/yr in 2012 (Jenkins et al., 2018). This decline may be primarily due to a significant drop in the temperature of modified CDW (mCDW) in 2012 and the retreat of the grounding line of the Kohler Glacier, which feeds the DIS (Scheuchl et al., 2016; Jenkins et al., 2018; Kim et al., 2021). Given the importance of iron-rich GMW for primary production, such large changes in GMW discharge may trigger variations in the GMW system, potentially causing significant impacts on the ecosystem in the ASP (Alderkamp et al., 2012; Arrigo et al., 2015). However, studies on the distribution of GMW in the ASP are sparse. Existing research has focused more on the warm period of the DIS in the summer of 2011 (Randall-Goodwin et al., 2015; Kim et al., 2016). Investigating GMW during the cool period of the DIS is valuable for providing more insights into the spatiotemporal variations of the GMW system in the ASP.

This study employed the method proposed by Randall-Goodwin et al. (2015) to quantify the proportions of subsurface GMW using potential temperature (θ), salinity, and dissolved oxygen (DO). Additionally, we estimated the contributions of meteoric water (MW) and sea ice meltwater (SIM) from $\delta^{18}O$ and salinity in seawater. In particular, we utilized radium isotopes ($^{226}Ra$ and $^{228}Ra$) to detect variations in GMW in surface waters, thereby addressing the limitations of noble gas tracers and hydrological parameters (θ, salinity and DO) in revealing surface GMW due to air-sea interaction (Stanley et al., 2009; Zheng et al., 2021). By combining the distributions of subsurface and surface GMW, we explored the sources and transport routes of GMW in the ASP. Furthermore, we compared our 2020 results with those reported in 2011 (Randall-Goodwin et al., 2015; Kim et al., 2016) to elucidate changes in the GMW distribution in the ASP after the DIS entered a cool period.

## 2. Materials and methods

### 2.1. Study area

Our study area is located in the western part of the Amundsen Sea within the eastern Pacific sector of the Southern Ocean (Fig. 1). Under the combined influence of solar radiation and katabatic winds, the ASP appears periodically in November and persists until March of the following year (Arrigo et al., 2012). Warm CDW with typical temperatures above 3.5 °C from the mid-layer of the Antarctic Circumpolar Current (ACC) intrudes onto the continental shelf via the Dotson Trough (DT) and Central Trough (CT), subsequently enhancing the basal melting of coastal ice shelves (Jacobs et al., 2011; Arneborg et al., 2012; Martinson, 2012; Schmidtko et al., 2014).

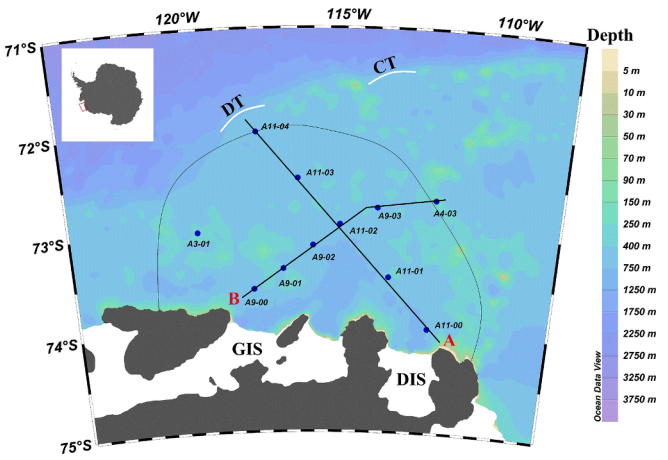


**Fig. 1.** Sampling locations for DO, $\delta^{18}O$, surface $^{226}Ra$, and $^{228}Ra$ determinations in the ASP. Note that no radium sample was collected at station A9-03. The upper map illustrates the ASP location in Antarctica (red box). The thin black curve indicates the approximate location of the sea ice edge in the ASP during the January-February 2020 sampling period. The nearly perpendicular lines represent transects A and B. The white curves indicate the approximate locations of Dotson Trough (DT) and Central Trough (CT). The bathymetry is shown in the background with a color bar on the right of the map. Coastal ice shelves are labeled: DIS for Dotson Ice Shelf and GIS for Getz Ice Shelf. This map was created using Ocean Data View (ODV; Schlitzer, 2018).

### 2.2. Sampling

In January 2020, the 36th Antarctic Scientific Expedition of China conducted a comprehensive survey of the Amundsen Sea aboard R/V *Xuelong*. A total of 11 CTD casts were performed on the continental shelf, forming two sections, A and B (Fig. 1). Section A extends northwest from the front of the DIS (station A11-00) to the shelf break (station A11-04) along the DT. Section B extends northeast from the front of the GIS (station A9-00) to the CT (station A4-03). Note that station A4-03 is located outside the ASP to the east, while the other stations are within the ASP (Fig. 1).

Seawater samples for DO and $\delta^{18}O$ measurements were collected using CTD rosettes at all stations. Approximately 125 mL of the DO sample was promptly transferred from the sampler to a brown glass bottle to prevent air contamination. Immediately, 1 mL of 2.4 M $MnCl_2$ solution and 1 mL of 1.8 M alkaline KI solution (in 5.4 M NaOH) were added to the sample. After thorough shaking, the $O_2$ reacted with $Mn^{2+}$ and $OH^-$ to form brown precipitates of high-valence manganese ($MnO(OH)_2$), which were used for subsequent analysis. Following DO sampling, the $\delta^{18}O$ sample was quickly transferred to a 2 mL glass vial. Ensuring the vial was free of air bubbles, the bottle mouth was sealed with a silicone gasket, stored at 4 °C and transported to an onshore laboratory.

Samples for radium isotope analysis were only collected from surface water, at an approximate depth of 10 m using a navigational sampling system. Samples were collected from 9 stations, excluding station A9-03. Briefly, a seawater sample (180 L) was transferred to a PVC bucket and then passed through a PVC tube filled with 12 g of polypropylene fiber coated with $MnO_2$ at a flow rate of 250 mL/min to concentrate radium. Preliminary experiments indicated that $MnO_2$-coated fiber achieves over 90 % efficiency in radium enrichment from seawater at this flow rate (Li et al., 2017). After enrichment, the Ra-enriched $MnO_2$-fiber was sealed in a plastic bag and transported to the onshore laboratory for radioactivity analysis of $^{226}Ra$ and $^{228}Ra$.

### 2.3. Measurements

#### 2.3.1. Temperature and salinity

Temperature, salinity, and depth were measured *in-situ* using a CTD equipped with dual sensors (Sea-Bird Scientific SEB 911 plus). The measurement accuracies for temperature and conductivity were 0.001 °C and 0.0003 S/m, respectively. The data are presented in Table S1.

#### 2.3.2. DO

DO was determined by the iodometric method with an automatic potentiometric titrator (Mettler Toledo-T50, Switzerland) on board. Briefly, 1 mL of 1: 3 (v/v) $H_2SO_4$ was added to dissolve the precipitate and oxidize $I^-$ to $I_2$ after the precipitate settled at the bottom of the brown glass bottle. The $I_2$ and corresponding DO content were measured by sodium thiosulfate titration. The sodium thiosulfate solution (ca. $1 \times 10^4$ μmol/L) was added to the sample by the automatic potentiometric titrator until the titration endpoint was reached. The DO concentration was calculated based on the volume of sodium thiosulfate solution consumed. The measurement accuracy of DO is ± 0.3 μmol/kg. The data are listed in Table S1.

#### 2.3.3. $\delta^{18}O$ in seawater

The oxygen isotopic compositions in seawater were analyzed using wavelength−scanning cavity ring-down spectroscopy (WS-CRDS) in a laser spectroscopy analyzer (Picarro L2140-I, USA) (Skrzypek and Ford, 2014). To avoid sample cross-contamination, each sample was analyzed through eight injections, and the average of the last five injections was used for calculation (Li et al., 2017; Wang et al., 2020). During measurements, three laboratory reference standards were included in the sample array for simultaneous measurement to ensure data quality. These standards were periodically calibrated against the Vienna Standard Mean Ocean Water (VSMOW) and the Standard Light Antarctic Precipitation (SLAP) provided by the International Atomic Energy Agency (IAEA). The $\delta^{18}O$ values reported here are expressed as $\delta^{18}O$ relative to VSMOW in units of ‰:

$$\delta^{18}O = \left[\frac{(^{18}O/^{16}O)_{sample}}{(^{18}O/^{16}O)_{VSMOW}} - 1\right] \times 10^3 \quad (1)$$

where $^{18}O/^{16}O$ represents the atomic ratio of $^{18}O$ to $^{16}O$.

The analytical precision of $\delta^{18}O$ is better than ± 0.03 ‰ based on duplicate measurements. The data are listed in Table S1.

#### 2.3.4. $^{226}Ra$ and $^{228}Ra$

The radioactivity concentrations of $^{226}Ra$ were determined by measuring $^{222}Rn$ ($T_{1/2}$ = 3.8 d) produced by the decay of $^{226}Ra$ (Xie et al., 1994; Li et al., 2017). Briefly, the $MnO_2$-coated fiber was sealed in a glass tube to accumulate $^{222}Rn$. After 5–7 days, the $^{222}Rn$ was transferred to a pre-evacuated scintillation cell coating with silver-activated zinc sulfide (ZnS [Ag]). After being stored for 3 h to allow the production of short-lived daughters ($^{218}Po$, $^{214}Pb$, $^{214}Bi$ and $^{214}Po$), α particles in the cell were counted using an Rn − Th analyzer (FD-125, Beijing Nuclear Instrument Factory, China). Each sample was measured at least twice, and the average value was taken as the activity concentration of $^{226}Ra$.

The radioactivity concentrations of $^{228}Ra$ were determined by measuring the β radiation of its short-lived daughter, $^{228}Ac$ ($T_{1/2}$ = 6.13 h) (Xie et al., 1994; Li et al., 2017). After determining $^{226}Ra$, radium was removed from $MnO_2$-coated fiber using a combination of hydroxylamine hydrochloride and hydrochloric acid, followed by co-precipitation with $Ba(Pb)SO_4$ (Moore, 1987). After standing overnight, the precipitate was centrifuged and dissolved in 8 mL of 0.5 M EDTA solution. The $BaSO_4$ precipitate was re-formed by adding 15 mL of $H_2SO_4$ (1 : 1) and re-dissolved in 8 mL of 0.5 M DTPA solution. The solution was left for at least 48 h to allow $^{228}Ac$ and $^{228}Ra$ to achieve radioactive equilibrium. Subsequently, radium was removed from solution by adding 1.4 M $Na_2SO_4$ to produce $Ba(Ra)SO_4$ precipitate. $^{228}Ac$ was extracted into chloroacetic acid solution and back-extracted into dilute nitric acid (1 : 14). Finally, $^{228}Ac$ was co-precipitated by $Ce_2(C_2O_4)_3$. The precipitate was dried and placed in a low background β counter (GM-25–5, Nuclear Technology Center, Technical University of Denmark) for $^{228}Ac$ determination.

### 2.4. Calculations

#### 2.4.1. Activity concentrations of $^{226}Ra$ and $^{228}Ra$

The activity concentrations of $^{226}Ra$ were calculated using the following formula (Xie et al., 1994):

$$A_{226} = \frac{k_{222} \times (N_s - N_b)}{\alpha \cdot V \cdot \eta \cdot t} \quad (2)$$

where $A_{226}$ represents the activity concentration of $^{226}Ra$ in the seawater sample (Bq/m$^3$). $k_{222}$ is the counting coefficient of $^{222}Rn$ (Bq/cpm). $N_s$ and $N_b$ refer to the total counts of the sample and background, respectively. $\alpha$ is the ingrowth coefficient of $^{222}Rn$. $V$ is the sample volume (m$^3$). $\eta$ is the emanation efficiency of $^{222}Rn$ from $MnO_2$-coated fiber, and $t$ is the counting time (min), which was identical for the sample and the background. The values of $k_{222}$ and $\eta$ were determined using a standard solution of $^{226}Ra$ with a known activity concentration. The value of $\eta$ was determined to be 91 ± 1.1 % (±1SD, n = 6). The activity concentrations of $^{226}Ra$ in this study are listed in Table 1. Error propagation was taken into account during the calculations.

The activity concentrations of $^{228}Ra$ were calculated using the following formula (Xie et al.,1994):

$$A_{228} = \frac{e^{\lambda \cdot \Delta t} \times (N_s - N_b)}{V \cdot \eta \cdot t} \quad (3)$$

where $A_{228}$ represents the activity concentration of $^{228}Ra$ in the seawater sample (Bq/m$^3$). $N_s$ and $N_b$ denote the total counts of the sample and background, respectively. λ is the decay constant of $^{228}Ac$, $\Delta t$ is the decay time of $^{228}Ac$ (i.e., the time from separation from $^{228}Ra$-$^{228}Ac$ equilibrium system to detection), $V$ is the sample volume (m$^3$), $t$ is the counting time (min), which is identical for both the sample and the background, and $\eta$ is the radiochemical recovery of $^{228}Ac$ in our experimental procedure, determined to be 47.7 ± 8.1 % (±2SD) by five different $^{228}Ra$ standard solutions (Table S2). The $^{228}Ra$ activity for each station is listed in Table 1. Error propagation was considered during the calculations.

#### 2.4.2. Proportion of GMW

The proportions of GMW were calculated based on the model employed by Randall-Goodwin et al. (2015). Briefly, the model assumes that seawater properties (θ, S, and DO) remain conservative when GMW mixes with ambient seawaters. Thus, the proportion of GMW in the mixture can be evaluated using these properties after determining the endmembers of all components. In surface layers, θ and DO are non-

**Table 1**
Activity concentration of radium isotopes in the ASP.

| Station | $^{226}Ra$ (Bq/m$^3$ ± 2SD) | $^{228}Ra$ (Bq/m$^3$ ± 2SD) |
|---|---|---|
| A11-00 | 0.56 ± 0.06 | 0.31 ± 0.07 |
| A11-01 | 1.19 ± 0.10 | 0.22 ± 0.06 |
| A11-02 | 1.35 ± 0.12 | 0.18 ± 0.05 |
| A11-03 | 2.48 ± 0.12 | 0.13 ± 0.05 |
| A11-04 | 0.61 ± 0.06 | 0.03 ± 0.03 |
| A3-01 | 0.63 ± 0.08 | 0.18 ± 0.05 |
| A4-03 | 1.52 ± 0.10 | 0.14 ± 0.04 |
| A9-00 | 0.78 ± 0.08 | 0.13 ± 0.05 |
| A9-01 | 0.95 ± 0.08 | 0.22 ± 0.05 |
| A9-02 | 1.47 ± 0.10 | 0.18 ± 0.04 |

conservative due to atmospheric influences via heat conduction and gas exchange. Consequently, the model is only applicable below the mixed layer (Jenkins, 1999).

In the ASP, mCDWs melt the basal DIS and further entrain GMW into the winter water (WW) layer, resulting in subsurface water being a mixture of mCDW, GMW and WW. To estimate the proportion of GMW using the model, the three endmembers of mCDW, GMW, and WW need to be determined. We used the averages of the mCDW properties (i.e., θ, S, and DO) as the mCDW endmember values (Fig. 2 and Fig. 3). The GMW endmember values were based on the values used in the same region by Randall-Goodwin et al. (2015). Since the WW we observed had been mixed with melt-laden mCDW (outflows carrying GMW), we used pure winter water (pWW) introduced by Jenkins et al. (2018) as the final endmember, which was also adopted in the study by Biddle et al. (2019). Fig. 2 shows the variations of θ and S for different water masses in our study. The endmember values of θ and S for pWW were determined by extrapolating WW to the freezing temperature line (Jenkins et al., 2018; Biddle et al., 2019). Biddle et al. (2019) demonstrated that GMW proportions were closer to those calculated from noble gases in the Amundsen Sea when using 80 % saturation DO concentration as the DO endmember value of pWW. Therefore, we used the 80 % saturation concentration at the measured temperature and salinity as the DO endmember value for pWW. The DO value of pWW is expected to be slightly higher than that of WW (Fig. 3a). The values of all endmembers are summarized in Table 2.

The proportions of GMW were calculated using equations (4) and (5) (Jenkins, 1999):

$$\psi^{1,2} = \left(\chi^2 - \chi^2_{mCDW}\right) - \left(\chi^1 - \chi^1_{mCDW}\right)\cdot\left(\chi^2_{pWW} - \chi^2_{mCDW}\right) \Big/ \left(\chi^1_{pWW} - \chi^1_{mCDW}\right) \tag{4}$$

$$f_{GMW} = \frac{\psi^{1,2}}{\psi^{1,2}_{GMW}} \tag{5}$$

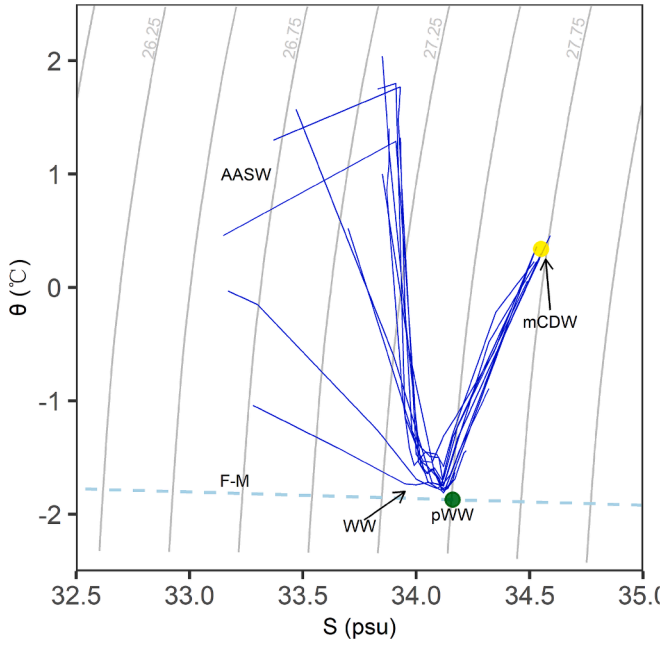


**Fig. 2.** The θ versus S plot for all stations in this study (one blue line for one station). The mCDW and pWW endmembers used for the GMW proportion calculation are highlighted by yellow and green circles, respectively. Antarctic Surface Water (AASW) and Winter Water (WW) are also shown. Grey lines in the background represent potential density ($\sigma_\theta$) isolines, ranging from 1026.00 to 1028.00 kg/m$^3$ in 0.25 kg/m$^3$ increments. The surface freezing temperature line is depicted by a light blue dashed line (F-M).

where $\chi$ represents the measured or endmember values of water samples or water masses; superscripts 1 and 2 denote distinct seawater properties (e.g., θ, S, and DO); subscripts indicate water masses (i.e., mCDW, pWW, and GMW); $\psi$ is a composite parameter calculated using θ, S, and DO, representing the relative content of GMW in the water sample; and $f_{GMW}$ is the proportion of GMW in the water sample. The calculation results are listed in Table S1. Further details regarding the model are provided in the supplementary material.

### 2.4.3. Proportions of MW and SIM

Proportions of MW and SIM were estimated from $\delta^{18}O$ and S following the methods described in Meredith et al. (2008, 2010, 2013) and Randall-Goodwin et al. (2015). In the ASP, salty mCDWs, characterized by an enrichment of heavy oxygen isotopes, continuously intrude onto the continental shelf. Meanwhile, MW, characterized by an enrichment of light oxygen isotopes, is introduced into the water column through glacial melting and precipitation. Additionally, sea ice formation and melting significantly influence salinity and, to a lesser extent, $\delta^{18}O$ through brine injection and SIM input (Macdonald et al., 1995; Meredith et al., 2013). Consequently, the distributions of salinity and $\delta^{18}O$ in seawater in the ASP are simultaneously controlled by the mixing of mCDW, MW and SIM (or brine released by sea ice formation, as indicated by a negative SIM proportion below). Given that salinity and $\delta^{18}O$ remain conservative during mixing, the MW and SIM proportions can be calculated using the mass balance of salinity and $\delta^{18}O$ by the following equations (6), (7), and (8) (Östlund and Hut, 1984):

$$f_{mCDW} + f_{SIM} + f_{MW} = 1 \tag{6}$$

$$f_{mCDW}\delta_{mCDW} + f_{SIM}\delta_{SIM} + f_{MW}\delta_{MW} = \delta \tag{7}$$

$$f_{mCDW}S_{mCDW} + f_{SIM}S_{SIM} + f_{MW}S_{MW} = S \tag{8}$$

where $f$ represents the proportion for each water mass; δ and S represent the $\delta^{18}O$ value and salinity, respectively, for water samples or water mass endmembers; the subscripts mCDW, SIM, and MW denote modified CDW, sea ice meltwater, and meteoric water, respectively.

To calculate the proportions of the MW, SIM, and mCDW in seawater, their endmember values were determined. Similar to the GMW calculation, the mean value of $\delta^{18}O$ of mCDW observed in this study was used as the endmember value of $\delta^{18}O$ (Fig. 3b). For the MW endmember, we referred to Randall-Goodwin et al. (2015) and Biddle et al. (2019), as the interannual variations of $\delta^{18}O$ in MW are small and are much smaller than the uncertainty of the mean MW endmember for the same area (Thomas et al. 2009; Meredith et al., 2013). Given the generally stable properties of sea ice, the SIM endmember used in this study is consistent with that in Randall-Goodwin et al. (2015). The endmembers of mCDW, MW, and SIM are summarized in Table 2, and the calculated results are listed in Table S1.

## 2.5. The distinction between the two mixing models

This study separately applies the GMW-mCDW-pWW and mCDW-MW-SIM mixing models for calculating GMW and MW/SIM proportions to different time scales. The GMW-mCDW-pWW mixing model addresses the mixing process on a relative short time scale, specifically when GMW mixes with ambient seawaters after being released from ice shelves, during which the properties (θ, S, and DO) remain conservative. In contrast, on a larger time scale, such as one year, θ, S, and DO are not solely governed by mixing but are significantly influenced by atmospheric interactions through heat conduction and gas exchange as the mixed layer deepens in winter (St-Laurent et al., 2015). Additionally, DO in water columns tends to be consumed during the remineralization of particulate organic matter (Karstensen et al., 2008). Therefore, the GMW proportion derived from this approach is effective only in the current summer. Conversely, the mCDW-MW-SIM mixing model is

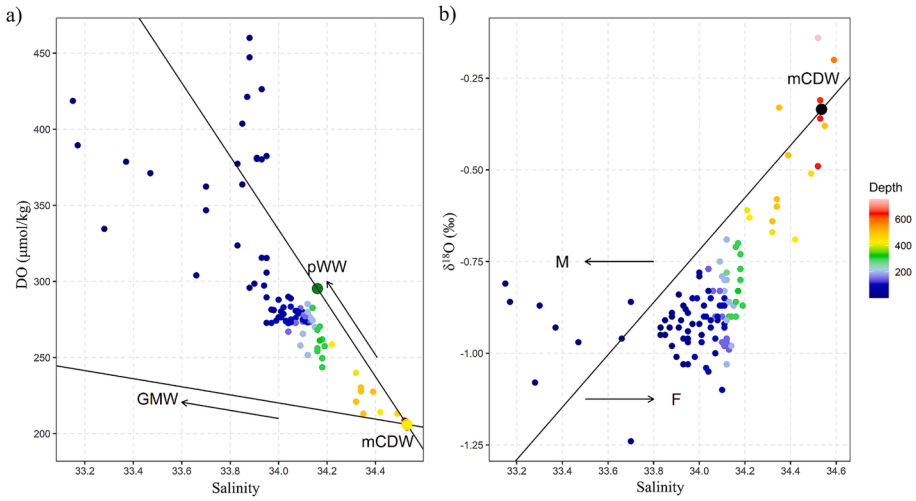


**Fig. 3.** Plots showing (a) DO versus salinity, with mixing lines between mCDW and pWW, and between mCDW and GMW, and (b) $\delta^{18}O$ versus salinity, with the mixing line between mCDW and MW. In panel (a), the pWW and mCDW endmembers used in this study are presented by larger green and yellow circles, respectively. In panel (b), deviations of data points from the mixing line are attributed to sea ice freezing (arrow F) and sea ice melting (arrow M); the mCDW endmember used in this study is represented by a black circle. Sample depths are color-coded according to the color bar on the right.

**Table 2**
The endmember characteristics of water masses in the ASP.

| water mass | parameter | | | |
|---|---|---|---|---|
| | θ (°C) | S (psu) | DO (μmol/kg) | $\delta^{18}O$ (‰) |
| mCDW | 0.30 | 34.53 | 206 | −0.34 |
| pWW | −1.87 | 34.16 | 295.3 | — |
| GMW | −89 | 0 | 1125 | −25 |
| SIM | — | 7 | — | 2.1 |
| MW | — | 0 | — | −25 |

applied in a longer time scale (e.g., one year), during which the distributions of salinity and $\delta^{18}O$ depend on the mixing of mCDW, SIM in summer (or brine released by sea ice formation in winter), and MW (GMW and precipitation). Consequently, the MW proportion derived from this model indicates the total inventory of GMW and precipitation over a relatively long period (Hennig et al., 2024).

## 3. Results

### 3.1. Distributions of θ, S and water masses

The water masses depicted in Fig. 2 are clearly identified by θ and S in Fig. 4. The mCDW is located below approximately 500 m, characterized by high potential temperatures (> 0 °C) and salinities (> 34.5). Due to the shallow water depth, the mCDW is thinner at the shelf break and at stations A9-03 and A4-03. Along transect A, from stations A11-04 to A11-00, the thickness of mCDW gradually increases, consistent with previous observations (Arneborg et al., 2012; Jacobs et al., 2012; Ha et al., 2014; Kim et al., 2021). Under the combined effects of solar radiation and sea ice melting, AASW exhibits the highest θ and the lowest salinity. For most water columns, WW occupies the depth range of 50–400 m, with homogeneous θ and S (θ ≈ −1.5 °C; S = 34.0 – 34.2) (Fig. 4). However, anomalous θ and S values were observed at some stations within the WW layer. For example, at stations A11-00 and A9-02, the potential temperatures in the WW layer slightly exceeded −1.5

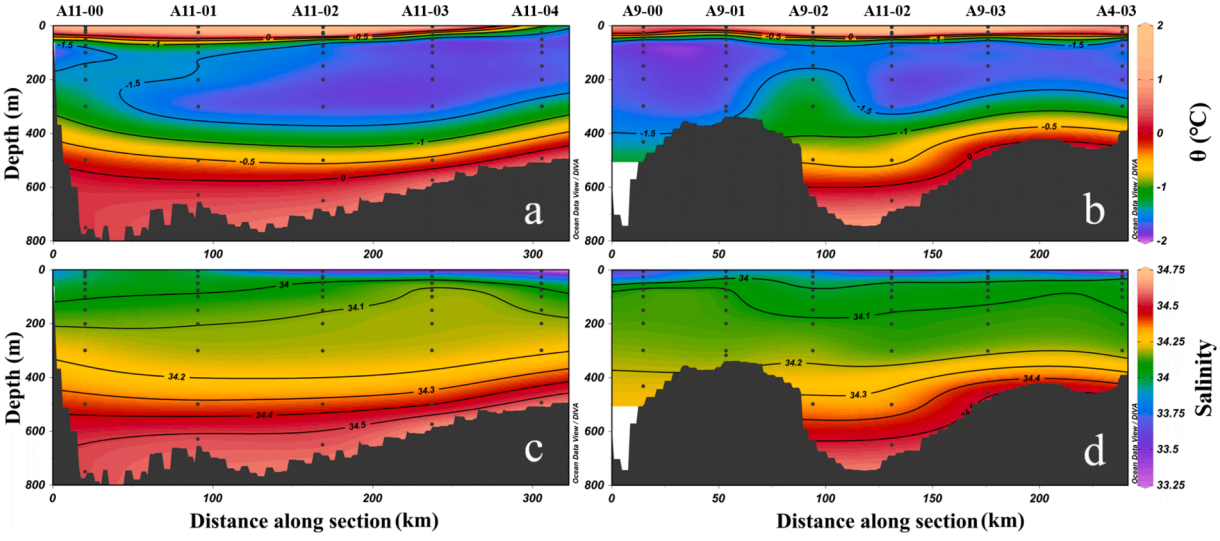


**Fig. 4.** Distributions of θ (a and b for transects A and B, respectively) and salinity (c and d for transects A and B, respectively). Contour lines of θ and S are labeled with their corresponding values. The scattered black dots indicate sampling depths. Station labels are displayed at the top of panels a and b. The plot was created using Ocean Date View (ODV; Schlitzer, 2018).

°C (Fig. 4a and 4b). In transect A, the salinity contour lines of 34.0 and 34.1 rise continuously from station A11-00 to A11-03 but abruptly deepen from station A11-03 to A11-04. Compared to the salinity contour line of 34.0, the 34.1 contour line shows greater variation along transect A, especially at station A11-03, where it forms a pronounced upward convexity (Fig. 4c). Similarly, along transect B, the depth variation of the 34.1 contour line is greater than that of 34.0, dropping suddenly from 75 m at station A9-01 to approximately 200 m at station A9-02 and maintaining a relatively deep depth between stations A9-02 and A4-03 (Fig. 4d).

### 3.2. Distributions of DO and $\delta^{18}O$

Fig. 3 illustrates that the variation in DO concentration with salinity is inversely related to that of $\delta^{18}O$. Generally, DO shows a negative correlation with salinity, reaching a minimum of 204.1 μmol/kg in the saltiest mCDW and maxima in the freshest AASW. In contrast, the $\delta^{18}O$ of mCDW is significantly higher than that of AASW and WW (Fig. 3b). Within the AASW, two distinct correlations between DO and S are observed: one indicates a broad range of DO variations with nearly constant salinity, reflecting net $O_2$ addition from the atmosphere, while the other shows a negative correlation between DO and salinity, indicating the combined influence of sea ice melting and air-sea exchange (Fig. 3a). In Fig. 3b, most samples deviate rightward from the mCDW-MW mixing line, suggesting the predominant influence of sea ice formation. Conversely, only a few AASW samples with the lowest salinities deviate leftward from the mixing line, reflecting the net effect of sea ice melt.

The sectional distributions of DO and $\delta^{18}O$ closely correspond to the distribution of water masses, providing detailed information at each station (Fig. 5). DO concentrations in the WW at stations A11-00, A11-01 and A11-02 range from 250 to 275 μmol/kg, showing lower levels compared to the northern stations A11-03 and A11-04 (Fig. 5a). The DO layer of 250–275 μmol/kg at station A11-02 is shallower and thinner compared to stations A11-00 and A11-01. Corresponding to the DO distribution, a high $\delta^{18}O$ tongue (> −0.9 ‰) in the WW layer extends from station A11-00 northward to A11-02 along transect A (Fig. 5c). In transect B, near station A11-02, station A9-02 also exhibits lower DO concentrations (<250–275 μmol/kg) and higher $\delta^{18}O$ (~ −0.8 ‰) in the WW layer compared to other stations in transect B (Fig. 5b and 5d).

### 3.3. Distributions of GMW, MW, and SIM

Fig. 6 presents the profiles of GMW proportions calculated using pairs of hydrological tracers (i.e., θ, S, and DO). In the mixed layer, the estimated GMW proportions show significant variability and lack consistency across the three tracer pairs due to atmospheric influences. Below the mixed layer, the three sets of GMW proportions generally agree well, except at stations A3-01, A9-00 and A9-01, where no GMW was detected. In this study, the mixed layer depth is defined as the depth below which the deviation between GMW proportions estimated from θ − S and θ − DO is less than 15 ‰. The GMW proportions presented here were averaged from the three sets of values derived from θ − S, θ – DO, and S − DO, respectively. These data are listed in Table S1.

Below the mixed layer along transect A, the GMW content gradually decreased northward from station A11-00 to A11-03 (Fig. 7a). Most of the GMW (proportion > 5 ‰) was concentrated in water columns with $\sigma_\theta < 27.45$ kg/m$^3$. Due to the uplift of $\sigma_\theta$ of 27.40 and 27.45 kg/m$^3$ from station A11-00 to A11-03, the layer enriched with GMW gradually thinned, with the GMW proportion decreasing from ~ 8 ‰ at station A11-00 to ~ 4 ‰ at station A11-03. Similarly, in transect B, GMW was mainly distributed in water columns with $\sigma_\theta < 27.45$ kg/m$^3$, except at stations A9-00 and A9-01 (Fig. 7b), where the GMW signals were unreliable (Fig. 6). Additionally, there were significant GMW enrichments in deeper waters with $\sigma_\theta > 27.45$ kg/m$^3$ at station A9-02, where the GMW proportion was 6.5–7.5 ‰, and at stations A9-03 and A4-03, where the GMW proportions were ~ 5 ‰ (Fig. 7b).

Similar to $\delta^{18}O$, MW was uniformly distributed in the AASW (Fig. 7c and 7d), likely reflecting the influence of surface precipitation. However, MW content in the WW exhibited distinct spatial variations. At station A11-03, MW contents were higher than at other stations (Fig. 7c). Notably, MW proportions at station A11-03 were significantly higher than at other stations within the water columns with $\sigma_\theta$ = 27.45–27.5 kg/m$^3$. In contrast, MW proportions at station A9-02 was significantly lower than at other stations at depths of 150–300 m (Fig. 7d).

The proportions of SIM are generally negative in the transects (Fig. 7e and 7f), reflecting the predominant influence of sea ice

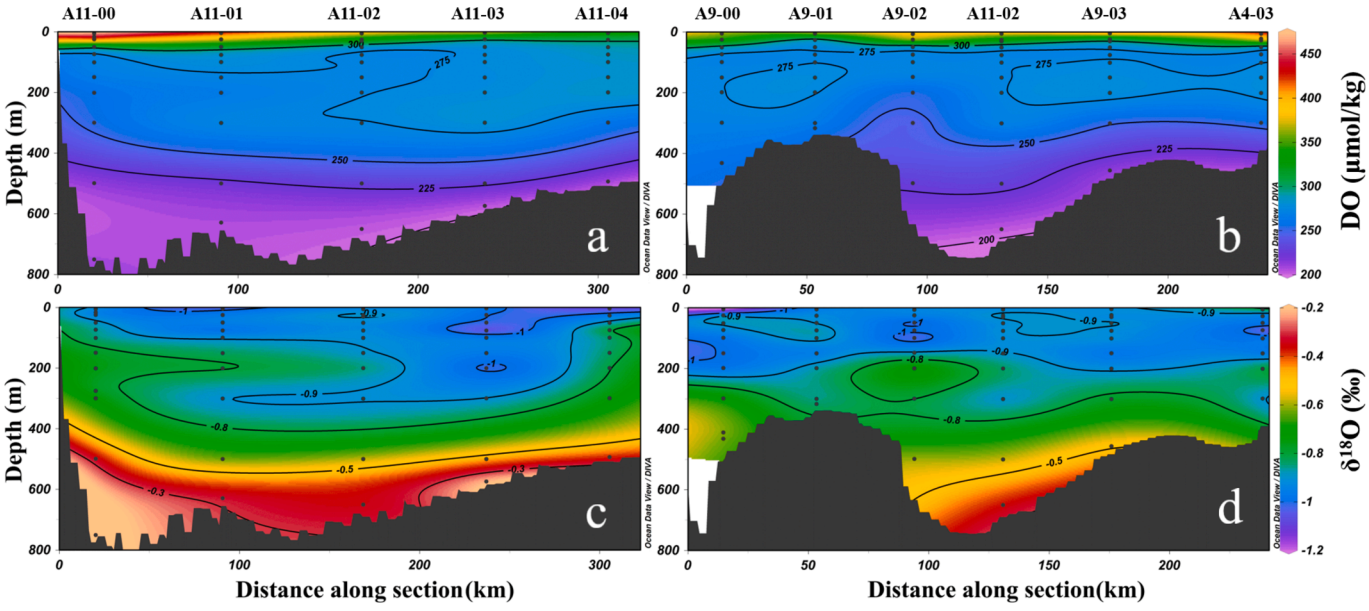


**Fig. 5.** Distributions of DO (a, b for transects A and B, respectively) and $\delta^{18}O$ (c, d for transects A and B, respectively). The contour lines of DO and $\delta^{18}O$ are labeled with corresponding values. The scattered black dots represent sampling depths. Station labels are shown at the top of panels a and b. The plot was created with Ocean Date View (ODV; Schlitzer, 2018).

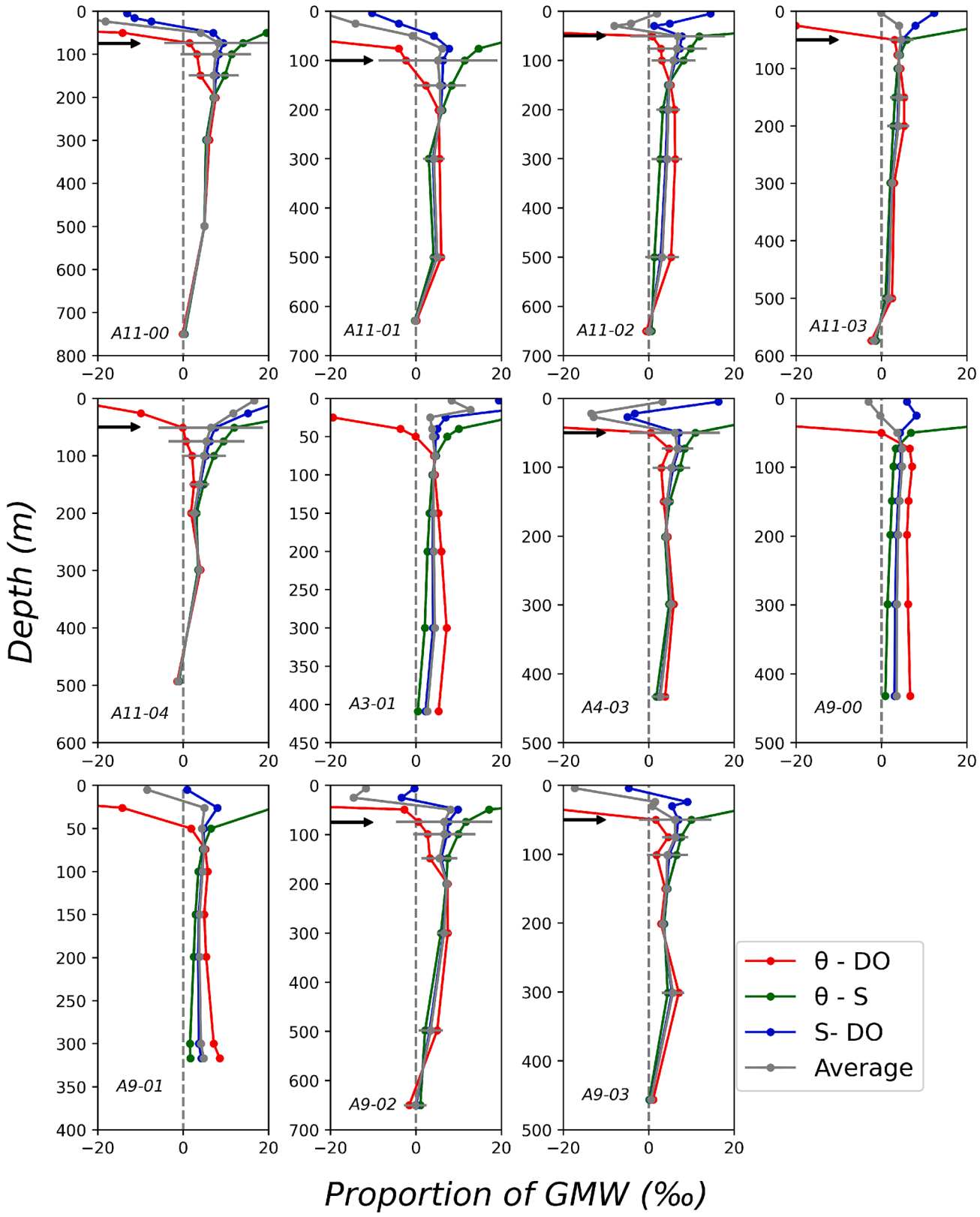


**Fig. 6.** Profiles of the GMW proportion estimated from θ − DO (red), θ − S (green), S − DO (blue), and their averages (grey) for each station. The corresponding stations are labeled at the bottom of each panel. Black arrows indicate the mixed layer depths for each station, except for stations A3-01, A9-00, and A9-01. Error bars representing ± 2SD of mean GMW proportions are shown below the marked depths.

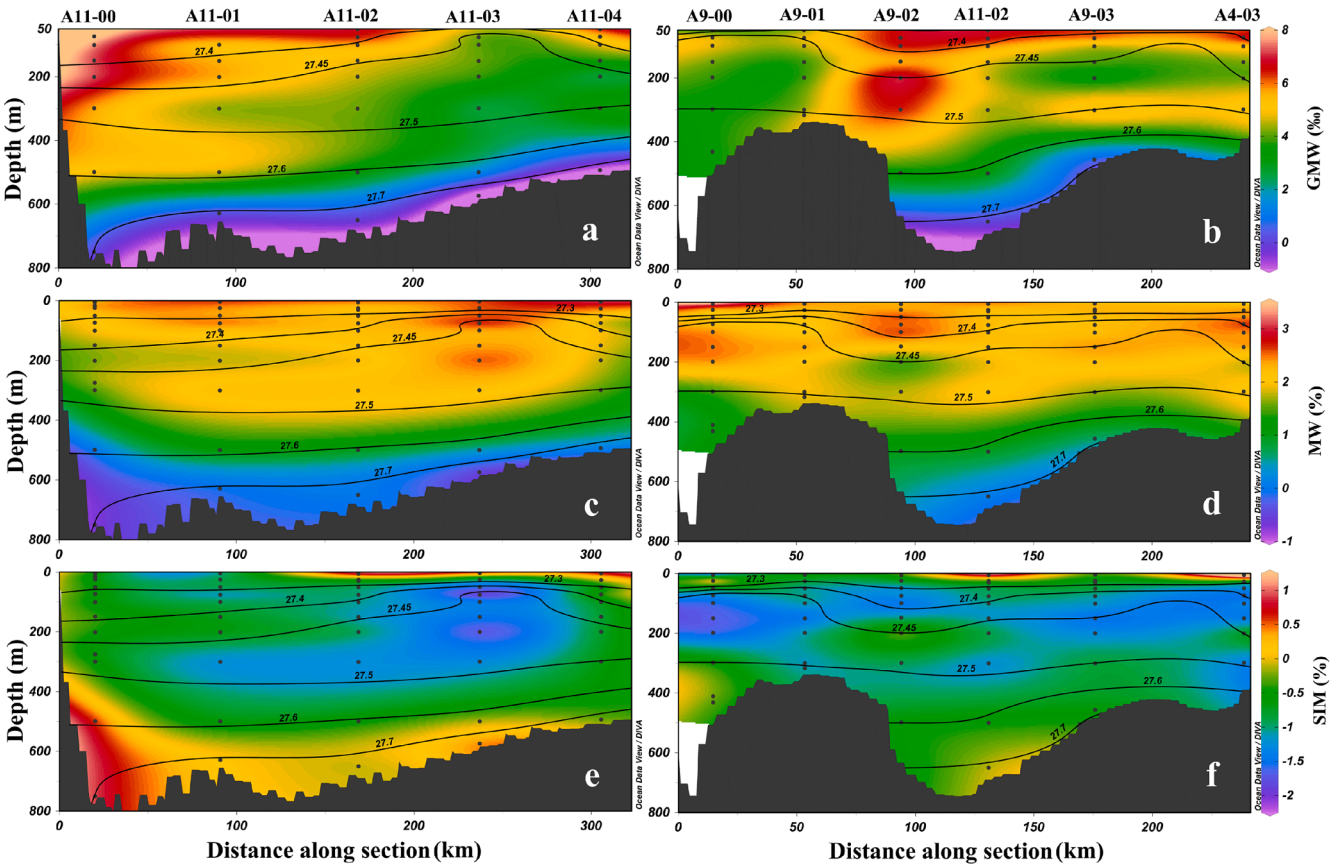


**Fig. 7.** Distributions of GMW (a, b for transects A and B, respectively), MW (c, d for transects A and B, respectively), and SIM (e, f for transects A and B, respectively). The contour lines of $\sigma_\theta$ are indicated by black lines with corresponding values. Scattered black dots represent sampling depths. Station labels are shown at the top of panels a and b. The plot was created using Ocean Date View (ODV; Schlitzer, 2018).

formation in the ASP, consistent with the preliminary analysis based on $\delta^{18}O$ and S in Fig. 3b. Brines (indicated by negative SIM proportions) released by sea ice formation in winter were heterogeneously distributed in the WW layer, indicating varying intensities of sea ice formation at the sea surface. For example, the brine was more enriched in the WW at station A11-03 compared to other stations in transect A, reflecting a stronger influence of sea ice formation during the last winter (Fig. 7e). Conversely, more positive SIM proportions at depths of 150–300 m at station A9-02 indicate a lesser influence of sea ice formation compared to other stations in transect B (Fig. 7f).

### 3.4. $^{226}Ra$ and $^{228}Ra$ in surface water

In transect A, the activity concentration of $^{226}Ra$ gradually increased away from the DIS, peaking at station A11-03 with a value of 2.48 ± 0.12 Bq/m$^3$, before sharply decreasing to 0.61 ± 0.06 Bq/m$^3$ at station A11-04 (Fig. 8a). The $^{226}Ra$ activity concentration at station A11-03 was significantly higher than at other stations, being approximately 1 Bq/m$^3$ greater than the second highest concentration at station A4-03 (1.52 ± 0.10 Bq/m$^3$). The lowest $^{226}Ra$ active concentration (0.56 ± 0.06 Bq/m$^3$) was observed at station A11-00, located near the front of the DIS. In transect B, the $^{226}Ra$ activity concentration was higher at three stations in the northeast (>1.00 Bq/m$^3$, A9-02, A11-02, and A4-03) compared to the other two stations. Station A3-01, located in the northwest of the ASP, also exhibited a low $^{226}Ra$ activity concentration of 0.63 ± 0.08 Bq/m$^3$ (Fig. 8a).

The activity concentration of $^{228}Ra$ gradually decreased northward along transect A, with the highest value observed at station A11-00 (0.31 ± 0.07 Bq/m$^3$) and the lowest at station A11-04 (0.03 ± 0.03 Bq/m$^3$) (Fig. 8b). In transect B, the highest $^{228}Ra$ concentrations were found in the center of the ASP, ranging from 0.18 to 0.22 Bq/m$^3$, while lower concentrations were recorded at the ends of the transect, specifically 0.13 ± 0.05 at station A9-00 and 0.14 ± 0.04 Bq/m$^3$ at station A4-03. Additionally, station A3-01 in the northwest of the ASP exhibited a higher $^{228}Ra$ activity concentration of 0.18 ± 0.05 Bq/m$^3$ (Fig. 8b).

## 4. Discussion

### 4.1. Sources and transport of subsurface GMW

Previous studies have observed a northward outflow in the west of the DT in the ASP with lower potential temperature and salinity than the inflowing mCDW. This has been attributed to the overturning of the mCDW inflow after the addition of GMW (Ha et al., 2014). Randall-Goodwin et al. (2015) also identified a strong outflow at depths > 400 m at the western end of the DIS, characterized by abnormally high temperatures, which they termed “melt-laden mCDW” following Jenkins (1999). We adopt the same terminology to refer to the GMW-containing outflows.

The distribution of GMW proportions estimated in this study clearly delineates the transport path of the melt-laden mCDW exported from the DIS basal cavity. After leaving the ice cavity, the melt-laden mCDW flows northwestward along the DT. The upper outflows are uplifted to depths shallower than 50 m along the $\sigma_\theta$ of 27.40–27.45 kg/m$^3$, while the lower outflows below $\sigma_\theta$ = 27.45 kg/m$^3$ remain at unchanged depths (Fig. 9 and 7a, b). Station A9-02 (73° 10.47́ S, 116°02.6́ W) is close to the M2 mooring station of Ha et al. (2014) (73°00.9́ S, 117°14.9́ W), where a significant outflow was observed. Consistently, we detected distinct signals of high θ, low DO, and high $\delta^{18}O$ in the subsurface water of station A9-02 (Fig. 4b, 5b, and 5d), suggesting it may be the core of

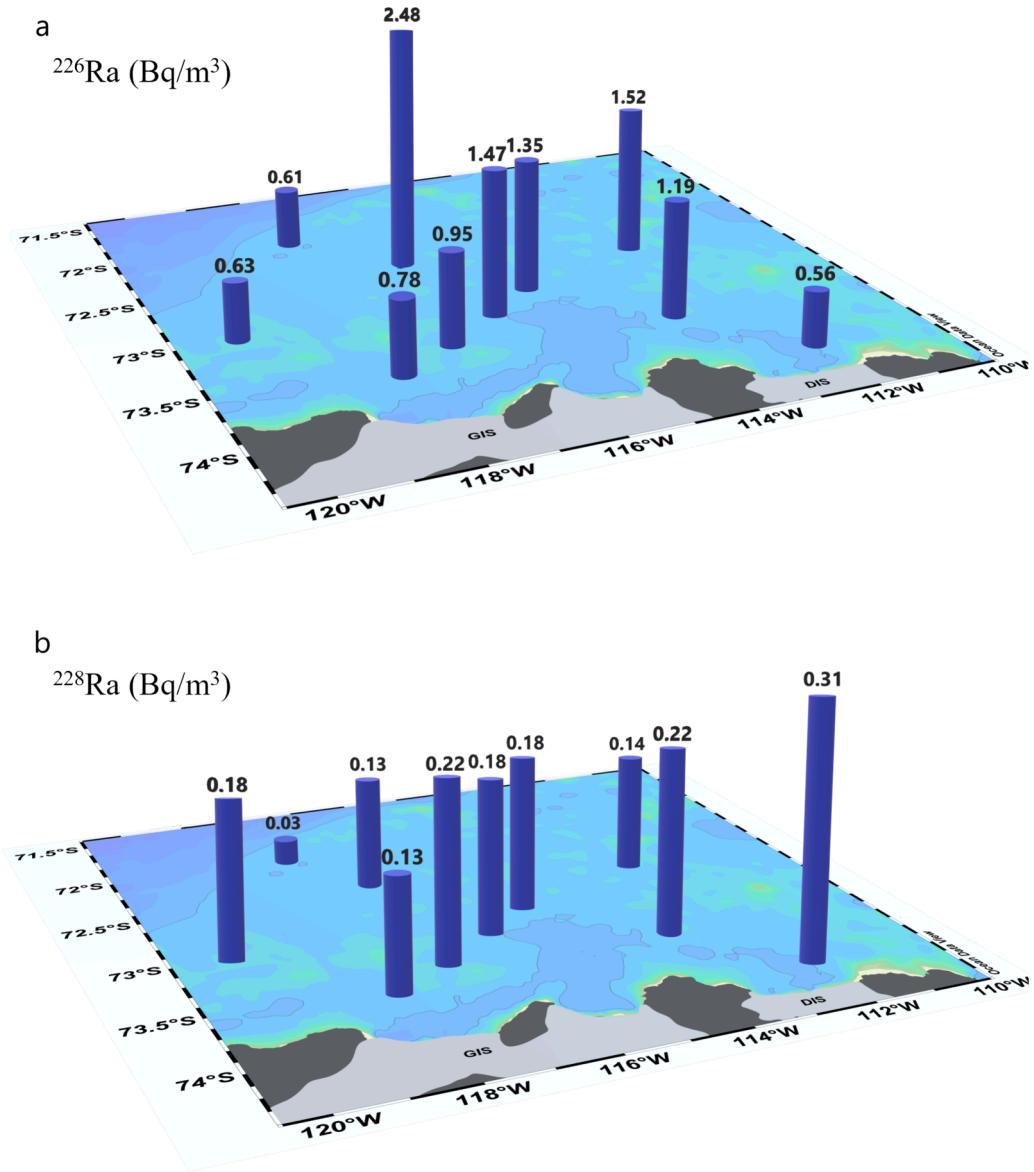


**Fig. 8.** Distribution of (a) $^{226}$Ra (Bq/m$^3$) and (b) $^{228}$Ra (Bq/m$^3$) in surface water. The activity concentrations of $^{226}$Ra and $^{228}$Ra are indicated above the corresponding bars, with their errors listed in Table 1. DIS and GIS refer to the Dotson Ice Shelf and Getz Ice Shelf, respectively.

the transport path of the melt-laden mCDW. This is further confirmed by the higher GMW proportions in subsurface water at station A9-02 (Fig. 7b and 9).

In comparison, stations A11-01 and A11-02 exhibit slightly higher DO concentrations, lower $\delta^{18}$O, and lower GMW proportions in the subsurface, implying that these stations may be at the edge of the outflow core (Figs. 5a, 5c, 7a and 9). Additionally, the sources of GMW at stations A9-03 and A4-03 may differ from other stations affected by GMW. Stations A9-03 and A4-03, located far from the core of the melt-laden mCDW (i.e., A9-02), have GMW contents that are slightly higher than station A11-02 at certain subsurface depths, suggesting that the GMWs at these westernmost stations are unlikely sourced from the DIS.

Our findings reveal two distinct layers enriched in GMW at stations A9-03 and A4-03: an upper layer at depths of 50–100 m and a lower layer at approximately 300 m (Fig. 7b and 9). This two-layer structure aligns with the GMW distribution pattern near the PIB in winter (Zheng et al., 2021) and corresponds with the GMW distribution near the Central Trough (CT), where GMW occupies water columns with $\sigma_\theta$ = 27.40 and 27.50 – 27.60 kg/m$^3$ (Biddle et al., 2019). The CT, located east of the ASP, plays a crucial role in channeling outflows from PIB to the open ocean (Biddle et al., 2019). Consequently, it is reasonable to infer that the GMWs at stations A9-03 and A4-03 originated from a branch of CT outflows from the PIB.

### 4.2. GMW in surface water traced by radium isotopes

In this study, we employed DO as one of parameters to quantitatively calculate the proportions of GMW. In addition to DO, noble gases were also used to track the transport of GMW (Hohmann et al., 2002; Loose and Jenkins, 2014; Beaird et al., 2015). DO and noble gases are effective tracers in subsurface waters for GMW. However, they are unreliable in surface waters due to air-sea exchanges of heat and gases, which introduce significant artifacts in the evaluation of GMW proportions, especially during the austral summer in Antarctica (Kim et al., 2016; Biddle et al., 2019; Zheng et al., 2021). Unlike DO and noble gases, radium isotopes are not significantly affected by atmospheric interactions and have the potential to trace GMW in surface waters if water masses in the ASP exhibit characteristic radium isotopes.

$^{226}$Ra has been widely used as a tracer for ocean circulations due to its long half-life ($T_{1/2}$ = 1602 a) (Ku and Luo, 1994; Hanfland, 2002).

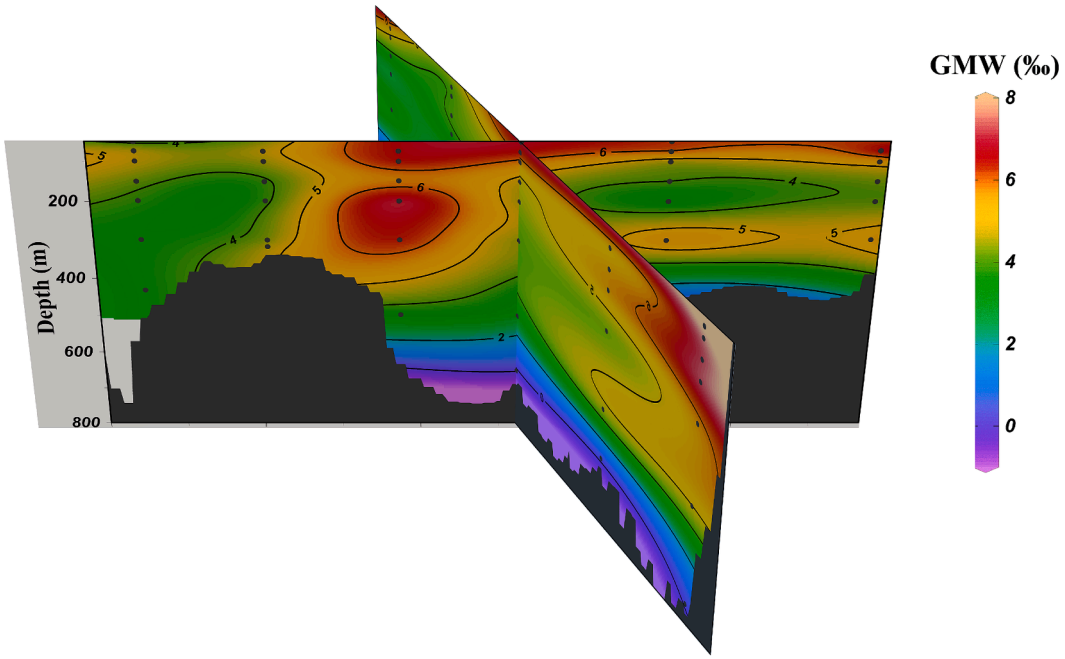


**Fig. 9.** Three-dimensional perspective distribution of GMW in the subsurface water in the ASP.

Observations in the Southern Ocean indicate that the activity concentration of $^{226}$Ra in CDW is around 3.00 Bq/m$^3$ (Ku et al., 1970; Ku and Lin, 1976; Chung, 1981; Bettoli et al., 1996), which is lower than that in the Atlantic Ocean, typically around 4.17 Bq/m$^3$ (Charette et al., 2015). Melt-laden mCDW forms through the mixing of CDW with WW and GMW. The mixture should maintain relatively high $^{226}$Ra activity because CDW is the dominant component, although the addition of WW and GMW with lower $^{226}$Ra activity may dilute it to some extent. Additionally, sediment release may increase the $^{226}$Ra activity concentrations in mCDW (Fig. 10a), resulting in elevated $^{226}$Ra activity in the mixtures (Kipp, 2018). The high $^{226}$Ra activity in melt-laden mCDW provides a means to trace its transport in the ASP.

Melt-laden mCDW was partly uplifted along the $\sigma_\theta$ = 27.40–27.45 kg/m$^3$ isopycnals during transport (Fig. 7a). This uplift may influence surface waters, leading to higher $^{226}$Ra concentrations compared to unaffected areas. Our results indicate that $^{226}$Ra activity concentrations along the transport path of melt-laden mCDW were higher than at stations without melt-laden mCDW (i.e., A3-01, A9-00 and A9-01 in Fig. 6), suggesting the impact of melt-laden mCDW on the surface waters at these stations, except for A11-00 and A11-04 (Fig. 8a). Notably, at station A11-03, where melt-laden mCDW was uplifted up to depths < 50 m (Fig. 7a), the $^{226}$Ra activity concentration was highest (2.48 ± 0.12 Bq/m$^3$), though still slightly lower than the typical $^{226}$Ra activity concentration of CDW. In contrast, even though station A11-00 had the highest GMW content in the water column (Figs. 9 and S1), the lowest $^{226}$Ra activity (0.56 ± 0.06 Bq/m$^3$) suggests minimal upwelling of melt-laden mCDW in front of the DIS, consistent with the deeper $\sigma_\theta$ = 27.45 kg/m$^3$ (Fig. 7a). The low $^{226}$Ra (0.61 ± 0.06 Bq/m$^3$) at station A11-04 may be due to dilution by SIM with extremely low $^{226}$Ra (Zheng et al., 2010), as A11-04 was at the edge of the ASP during sampling.

$^{228}$Ra is a shorter-lived radionuclide with a half-life of 5.75 years, and its activity in CDW is usually below the detection limit (Charette et al., 2007, 2015). Therefore, CDW cannot be a source of $^{228}$Ra in the ASP. In estuaries and continental shelves, $^{228}$Ra primarily originates from river inputs, seafloor sediments, and submarine groundwater discharges (Moore, 1987, 1998; Charette et al., 2013, 2016; Li et al., 2017; Kipp, 2018). However, in the coastal oceans of the Antarctic, $^{228}$Ra is generally supplied by sediments at the bottom of ice shelves, where it dissolves in GMW and is transported into the oceans via GMW outflows (Yager et al., 2012; Vernet et al., 2012; Annett et al., 2013; Herraiz-Borreguero et al., 2016). This single source of $^{228}$Ra makes it a useful tracer for GMW transport, especially in surface waters due to reduced influence from seafloor sediments compared to deeper waters. In this study, the highest $^{228}$Ra activity concentration (0.31 ± 0.07 Bq/m$^3$) was

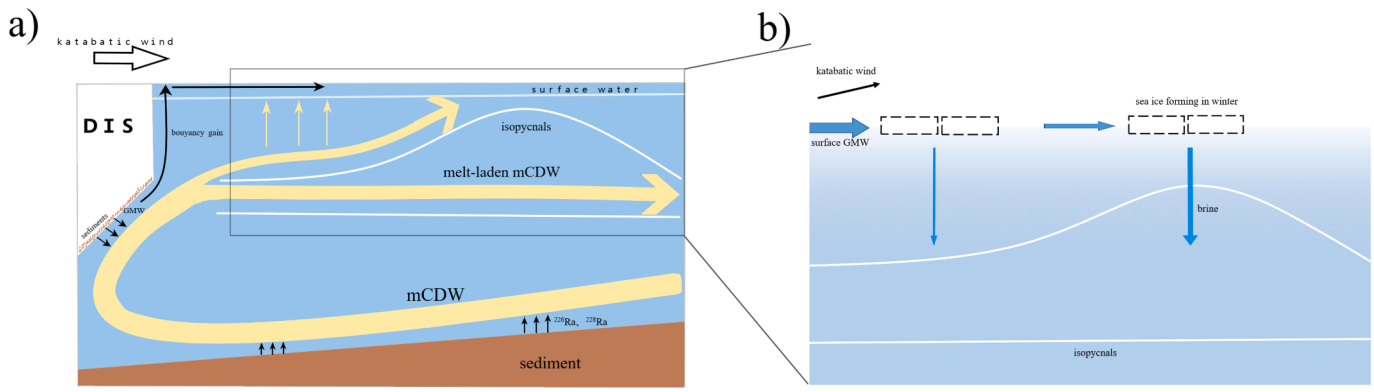


**Fig. 10.** Schematic of water mass transports and interactions along the DT transect (a), and the effect of sea ice formation on the $\sigma_\theta$ structure (b).

observed at station A11-00, which also had the lowest $^{226}$Ra activity (Fig. 8). Given A11-00's proximity to the DIS, it can be inferred that surface $^{228}$Ra at A11-00 was supplied by upwelling GMW from the basal ice cavity (Fig. 10a). These upwellings are consistent with observations in the PIB, where GMW from the basal ice cavity of PIIS was buoyantly uplifted to the surface (Zheng et al., 2021). Surface water transport in the ASP is predominantly controlled by northwesterly katabatic winds (Heywood et al., 2016; Kim et al., 2016; Kim et al., 2021). The northwestward decrease in surface $^{228}$Ra activity suggests wind-driven transport of surface GMW (Fig. 8b). The decline in $^{228}$Ra activity from the DIS front to the open ocean may result from dilution of SIM (e.g., A11-04) and upwelling of melt-laden mCDW (e.g., A11-03) (Fig. 10a).

### 4.3. Effects of sea ice formation on subsurface GMW transport paths

In the ASP, the brines released by sea ice formation ($f_{SIM} < 0$) in winter were primarily stored between $\sigma_\theta$ = 27.40 and 27.50 kg/m$^3$ during summer (Fig. 7e, f). Theoretically, the addition of brine increases salinity, thereby affecting $\sigma_\theta$ variations in seawater. To examine the relationship between sea ice formation and $\sigma_\theta$, brine inventories in the water columns from 50 to 300 m (approximately $\sigma_\theta$ = 27.40 to 27.50 kg/m$^3$) were calculated. The results indicate that the spatial variation of brine stocks aligns well with the depth variation of $\sigma_\theta$ = 27.40 and 27.45 kg/m$^3$ in both transects A and B (Fig. 11). Specifically, at stations with high brine stocks, the isopycnals of $\sigma_\theta$ are convex (e.g., A11-03) and concave at stations with low brine stocks (e.g., A9-02), suggesting that more brine released by sea ice formation leads to denser waters. During our sampling, part of the melt-laden mCDW was transported along the $\sigma_\theta$ = 27.40–27.45 kg/m$^3$ isopycnals (Fig. 7a, b). Consequently, sea ice formation influenced the transport paths of subsurface GMWs in the ASP (Fig. 10). Webber et al. (2017) proposed a mechanism by which increased sec ice production and surface heat loss affect CDW properties by deepening the thermocline on the shelf. Our study suggests that sea ice production may also impact the outflow of melt-laden mCDW. Silvano et al. (2018) suggested that GMW discharges reduce seawater salinity, which weakens sea ice formation. From this perspective, increased GMW inputs in a warming world may stabilize the GMW transport paths in the subsurface, as indicated by our study.

During winter sea ice formation, the released brines increase the density of surface seawater, resulting in an enrichment of meteoric water in the subsurface. As shown in Fig. 12, stations with high brine inventories, such as A11-01, A11-02, and A11-03, exhibited elevated MW contents in the water columns. The subsurface GMW content cannot fully explain these high MW inventories, as subsurface GMW was significantly lower than MW (Fig. S1). Therefore, we propose that most of the MW in the WW was enriched through the entrainment of brines during winter sea ice formation. Conversely, at station A11-00, where net sea ice melting occurred (indicated by a positive value of SIM), GMW was the main contributor to MW (Figs. 12 and S1). A11-00 was the only station with a positive SIM in the water column, possibly due to the upwelling of GMW suppressing sea ice formation (Zheng et al., 2021).

### 4.4. Changing GMWs in the ASP

Our study elucidates the sources and distribution of GMW in the ASP during the austral summer of 2020. By contrasting our findings with those of Randall-Goodwin et al. (2015) and Kim et al. (2016) from the summer of 2011, we aimed to identify changes in GMW in the ASP.

The first change is the properties of mCDW. The grounding line of the DIS in 2011 had not retreated, and the mCDW was warmer compared to 2020. In 2011, the characteristic temperature and salinity of the mCDW endmember were 0.75 °C and 34.62, respectively (Randall-Goodwin et al., 2015), consistent with the mCDW endmember in 2011 (θ and S were 0.85 °C and 34.61, respectively) observed by Jenkins et al. (2018). Our observations indicate that the characteristic θ and S of the mCDW endmember were 0.30 °C and 34.53, respectively, in the summer of 2020, aligning with the range after 2012 provided by Jenkins et al. (2018) (see their Supplementary Information). Compared to 2011, the DIS was in a cooler period in 2020 when we sampled.

The second change is the content of GMW. The proportions of

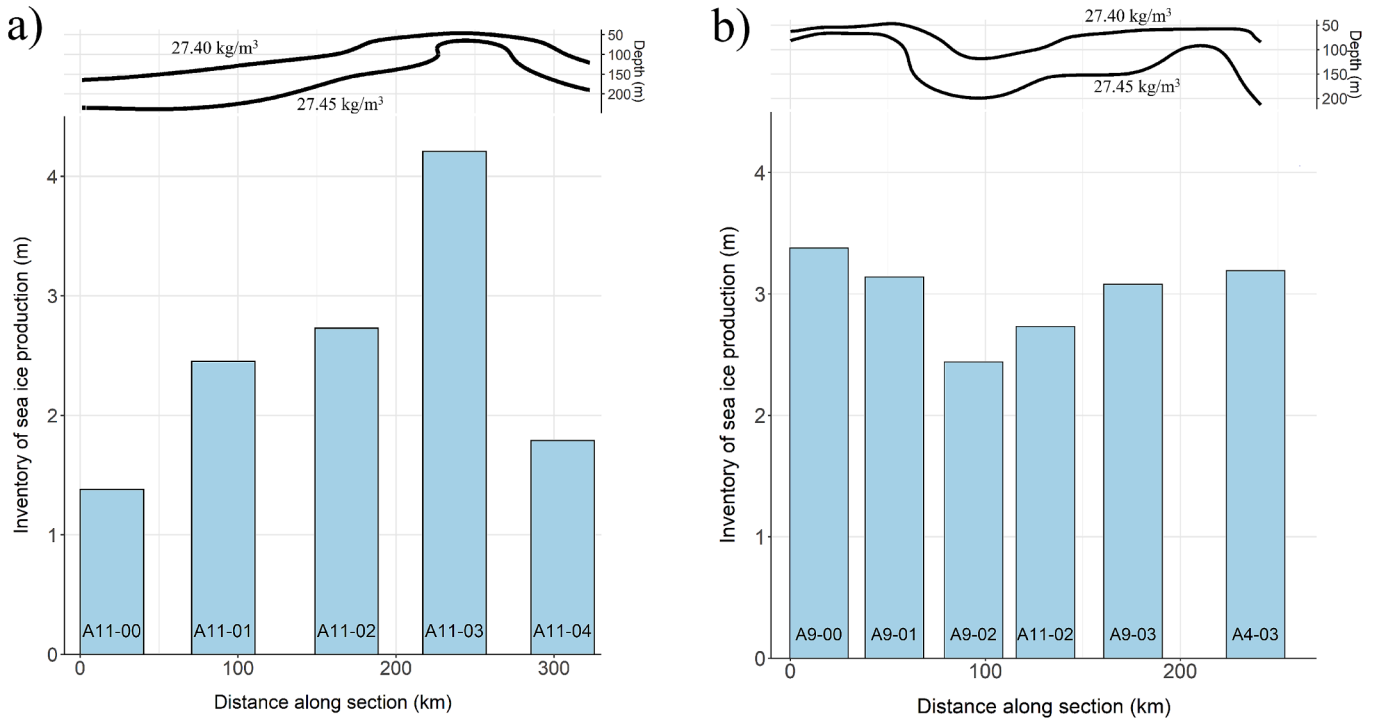


**Fig. 11.** Relationship between the depth of $\sigma_\theta$ = 27.40 to 27.50 kg/m$^3$ and brine inventory in 50–300 m water columns for each station in transects A (a) and B (b). The vertical bars represent brine inventories. Depth variations of $\sigma_\theta$ = 27.40 and 27.45 kg/m$^3$ along the transects are plotted above the corresponding subplots. Station numbers are labeled at the bottom of the bars.

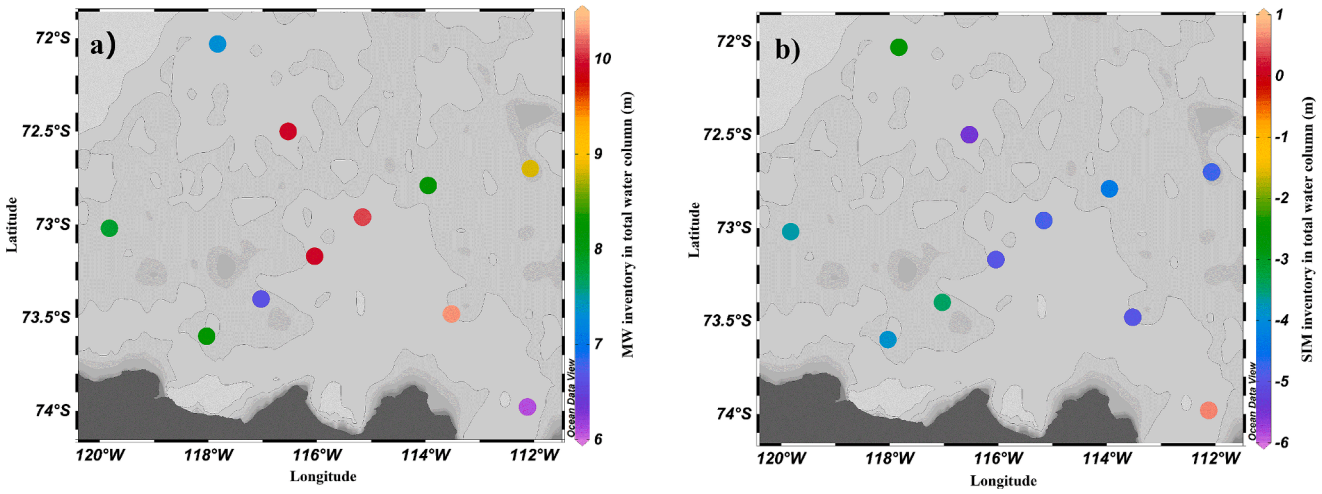


**Fig. 12.** Spatial distributions of MW (a) and SIM inventories (b) in the water column in the ASP. Note that negative SIM values indicate brines released by net sea ice formation.

subsurface GMW estimated by our approach in the summer of 2020 are generally below 8 ‰, whereas the maximum proportions of subsurface GMW in the ASP in 2011 exceeded 8 ‰ for most stations, reaching up to 12 ‰ in areas adjacent to A11-00 (Randall-Goodwin et al., 2015). This suggests that the GMW content in 2020 dropped to about half of what it was in 2011, which aligns with the reduction in DIS meltwater flux during the cooler period compared to 2011 (Jenkins et al., 2018; Kim et al., 2021).

The third change is in the transport route of GMW. In the summer of 2011, the depth of the highest subsurface GMW proportion generally increased with distance from the DIS (Randall-Goodwin et al., 2015). The distributions of the Ne and He tracers also indicated that subsurface GMWs from the DIS in the summer of 2011 mainly occupied depths of 200–700 m and tended to deepen northward along the $\sigma_\theta$ = 27.45–27.65 kg/m$^3$ (Kim et al., 2016). However, unlike in 2011, our results suggest that the subsurface GMW exported from the DIS partly upwelled along the $\sigma_\theta$ = 27.40–27.45 kg/m$^3$ during northward transport in the summer of 2020, implying a change in the transport route of GMW. We hypothesize that intensive sea ice formation released more brine into the WW layers in the winter of 2020, raising the depth of $\sigma_\theta$ = 27.40–27.45 kg/m$^3$ and consequently uplifting the subsurface GMW transport path.

Previous studies have demonstrated that freshwater inputs from glaciers hinder DSW formation by counteracting salt flux during sea ice formation (Williams et al, 2016; Amblas and Dowdeswell, 2018; Silvano et al., 2018). Modeling indicates that, in the absence of freshwater inputs, the salinity in the mixed layer in the ASP would be 0.3 psu higher than observed (Silvano et al., 2018). Consequently, the decreases in GMW input in the ASP after 2011 may increase the salinity of the mixed layer, enhancing the intensity of brine injections during winter sea ice formation. Controlled by the Amundsen Sea Low (Turner et al., 2013; Clem et al., 2017; Holland et al., 2018), the glacial meltwater system in the Amundsen Sea exhibits interannual and seasonal variability (Jenkins et al., 2018; Yang et al., 2022). Such changes in the glacial meltwater system in the ASP may affect the formation of AABW in the Ross Sea (Jacobs et al., 2022). Additionally, one question arises: how has the ASP ecosystem responded to these changes? To answer this question, further investigations are needed in the future.

## 5. Conclusions

In this study, we combined potential temperature, salinity, and dissolved oxygen to estimate the proportions of GMW in the subsurface water, while $^{226}$Ra and $^{228}$Ra were employed to trace the melt-laden mCDW and GMW in the surface water. Our results indicate a strong concordance between the distributions of GMW in the subsurface and surface waters. The GMW in the ASP is primarily sourced from the DIS and PIB. The GMW exported from the DIS basal ice cavity follows two transport pathways: one ascends to the surface at the front of the DIS due to buoyancy, and the other is transported in the subsurface layer along with the melt-laden mCDW. The surface GMW at the DIS front is driven northwestward by katabatic winds, while the subsurface GMW is transported northwestward beneath the mixed layer, with the upper portion upwelling to the surface in the center of the ASP along the isopycnal $\sigma_\theta$ = 27.40–27.45 kg/m$^3$. Most of the SIM proportions estimated from $\delta^{18}$O and salinity are negative, indicating that the ASP is predominantly influenced by strong sea ice formation during winter. The brine rejection from sea ice formation alters the depth distributions of $\sigma_\theta$ = 27.40–27.45 kg/m$^3$, thereby affecting the transport path of the subsurface GMW. Compared to the summer of 2011, the GMW content in the ASP decreased by nearly half by the summer of 2020, suggesting significant variability in the GMW system within the ASP.

## CRediT authorship contribution statement

**Guanghui Chen:** Data curation, Formal analysis, Methodology, Writing – original draft. **You Jiang:** Formal analysis, Methodology. **Yi Wang:** Formal analysis, Investigation. **Jun Zhao:** Formal analysis, Methodology. **Yusheng Qiu:** Methodology, Resources. **Minfang Zheng:** Resources, Software, Validation. **Mengya Chen:** Software, Visualization. **Jianming Pan:** Funding acquisition, Validation. **Min Chen:** Conceptualization, Data curation, Funding acquisition, Writing – review & editing.

## Declaration of competing interest

The authors declare that they have no known competing financial interests or personal relationships that could have appeared to influence the work reported in this paper.

## Acknowledgments

We express our gratitude to the two reviewers for their invaluable comments, and to the China Polar Research Center for providing temperature and salinity data. This study was funded by grants IRASCC 02-01-01 and IRASCC 01-01-02C from the Arctic and Antarctic Administration of China, as well as grants No. 41721005 and No. 41976228 from the National Natural Science Foundation of China.

## Appendix A. Supplementary material

Supplementary data to this article can be found online at https://doi.org/10.1016/j.pocean.2024.103367.

## Data availability

Data will be made available on request.

## References


Alderkamp, A.C., Mills, M.M., van Dijken, G.L., Laan, P., Thuróczy, C.E., Gerringa, L.J., de Baar, H.J., Payne, C.D., Visser, R.J., Buma, A.G., Arrigo, K.R., 2012. Iron from melting glaciers fuels phytoplankton blooms in the Amundsen Sea (Southern Ocean): Phytoplankton characteristics and productivity. Deep-Sea Res. Part II - Top. Stud. Oceanogr. 71, 32–48. https://doi.org/10.1016/j.dsr2.2012.03.005.

Alderkamp, A.C., van Dijken, G.L., Lowry, K.E., Connelly, T.L., Lagerström, M., Sherrell, R.M., Haskins, C., Rogalsky, E., Schofield, O., Stammerjohn, S.E., Yager, P. L., Arrigo, K.R., 2015. Fe availability drives phytoplankton photosynthesis rates during spring bloom in the Amundsen Sea Polynya. Elementa - Sci. Anthrop. 3, 000043. https://doi.org/10.12952/journal.elementa.000043.

Amblas, D., Dowdeswell, J.A., 2018. Physiographic influences on dense shelf-water cascading down the Antarctic continental slope. Earth-Sci. Rev. 185, 887–900. https://doi.org/10.1016/j.earscirev.2018.07.014.

Annett, A.L., Henley, S.F., van Beek, P., Souhaut, M., Ganeshram, R., Venables, H.J., Meredith, M.P., Geibert, W., 2013. Use of radium isotopes to estimate mixing rates and trace sediment inputs to surface waters in northern Marguerite Bay Antarctic Peninsula. Antarct. Sci. 25 (3), 445–456. https://doi.org/10.1017/S0954102012000892.

Arneborg, L., Wåhlin, A.K., Björk, G., Liljebladh, B., Orsi, A.H., 2012. Persistent inflow of warm water onto the central Amundsen shelf. Nat. Geosci. 5 (12), 876–880. https://doi.org/10.1038/ngeo1644.

Arrigo, K.R., Lowry, K.E., van Dijken, G.L., 2012. Annual changes in sea ice and phytoplankton in polynyas of the Amundsen Sea, Antarctica. Deep-Sea Res. Part II: Top. Stud. Oceanogr. 71, 5–15.

Arrigo, K.R., van Dijken, G.L., 2003. Phytoplankton dynamics within 37 Antarctic coastal polynya systems. J. Geophys. Res. - Oceans 108 (C8). https://doi.org/10.1029/2002JC001739.

Arrigo, K.R., van Dijken, G.L., Strong, A.L., 2015. Environmental controls of marine productivity hot spots around Antarctica. J. Geophys. Res. - Oceans 120 (8), 5545–5565. https://doi.org/10.1002/2015JC010888.

Assmann, K.M., Jenkins, A., Shoosmith, D.R., Walker, D.P., Jacobs, S.S., Nicholls, K.W., 2013. Variability of Circumpolar Deep Water transport onto the Amundsen Sea continental shelf through a shelf break trough. J. Geophys. Res. - Oceans 118 (12), 6603–6620. https://doi.org/10.1002/2013JC008871.

Beaird, N., Straneo, F., Jenkins, W., 2015. Spreading of Greenland meltwaters in the ocean revealed by noble gases. Geophys. Res. Lett. 42 (18), 7705–7713. https://doi.org/10.1002/2015GL065003.

Bettoli, M.G., Cantelli, L., Queirazza, G., Roveri, M., Tositti, L., Tubertini, O., Valcher, S., 1996. Distribution of $^{226}$Ra in the Ross Sea—Antarctica. Int. J. Environ. Anal. Chem. 63 (1), 29–36. https://doi.org/10.1080/03067319608039807.

Biddle, L.C., Heywood, K.J., Kaiser, J., Jenkins, A., 2017. Glacial meltwater identification in the Amundsen Sea. J. Phys. Oceanogr. 47 (4), 933–954. https://doi.org/10.1175/JPO-D-16-0221.1.

Biddle, L.C., Loose, B., Heywood, K.J., 2019. Upper ocean distribution of glacial meltwater in the Amundsen Sea. Antarctica. J. Geophys. Res. - Oceans 124 (10), 6854–6870. https://doi.org/10.1029/2019JC015133.

Boyd, P.W., Jickells, T., Law, C.S., Blain, S., Boyle, E.A., Buesseler, K.O., Coale, K.H., Cullen, J.J., de Baar, H.J., Follows, M., Harvey, M., Lancelot, C., Levasseur, M., Owens, N.P., Pollard, R., Rivkin, R.B., Sarmiento, J., Schoemann, V., Smetacek, V., Takeda, S., Tsuda, A., Turner, S., Watson, A.J., 2007. Mesoscale iron enrichment experiments 1993–2005: synthesis and future directions. Science 315 (5812), 612–617. https://doi.org/10.1126/science.1131669.

Castagno, P., Capozzi, V., DiTullio, G.R., Falco, P., Fusco, G., Rintoul, S.R., Spezie, G., Budillon, G., 2019. Rebound of shelf water salinity in the Ross Sea. Nat. Commun. 10 (1), 1–6. https://doi.org/10.1038/s41467-019-13083-8.

Charette, M.A., Gonneea, M.E., Morris, P.J., Statham, P., Fones, G., Planquette, H., Salter, I., Garabato, A.N., 2007. Radium isotopes as tracers of iron sources fueling a Southern Ocean phytoplankton bloom. Deep-Sea Res. Part II - Top Stud. Oceanogr. 54 (18–20), 1989–1998. https://doi.org/10.1016/j.dsr2.2007.06.003.

Charette, M.A., Henderson, P.B., Breier, C.F., Liu, Q., 2013. Submarine groundwater discharge in a river-dominated Florida estuary. Mar. Chem. 156, 3–17. https://doi.org/10.1016/j.marchem.2013.04.001.

Charette, M.A., Morris, P.J., Henderson, P.B., Moore, W.S., 2015. Radium isotope distributions during the US GEOTRACES North Atlantic cruises. Mar. Chem. 177, 184–195. https://doi.org/10.1016/j.marchem.2015.01.001.

Charette, M.A., Lam, P.J., Lohan, M.C., Kwon, E.Y., Hatje, V., Jeandel, C., Shiller, A.M., Cutter, G.A., Thomas, A., Boyd, P.W., Homoky, W.B., Milne, A., Thomas, H., Andersson, P.S., Porcelli, D., Tanaka, T., Geibert, W., Dehairs, F., Garcia-Orellana, J., 2016. Coastal ocean and shelf-sea biogeochemical cycling of trace elements and isotopes: lessons learned from GEOTRACES. Philos. Trans. R. Soc. A - Math. Phys. Eng. Sci. 374 (2081), 20160076. https://doi.org/10.1098/rsta.2016.0076.

Chung, Y., 1981. $^{210}$Pb and $^{226}$Ra distributions in the Circumpolar waters. Earth Planet. Sci. Lett. 55 (2), 205–216. https://doi.org/10.1016/0012-821X(81)90100-X.

Clem, K.R., Renwick, J.A., McGregor, J., 2017. Large-scale forcing of the Amundsen Sea Low and its influence on sea ice and West Antarctic temperature. J. Clim. 30 (20), 8405–8424. https://doi.org/10.1175/JCLI-D-16-0891.1.

Dinniman, M.S., Klinck, J.M., Hofmann, E.E., 2012. Sensitivity of Circumpolar Deep Water transport and ice shelf basal melt along the West Antarctic Peninsula to changes in the winds. J. Clim. 25 (14), 4799–4816. https://doi.org/10.1175/JCLI-D-11-00307.1.

Dutrieux, P., Rydt, J.D., Jenkins, A., Holland, P.R., Ha, H.K., Lee, S.H., Steig, E.J., Ding, Q., Abrahamsen, E.P., Schröder, M., 2014. Strong sensitivity of Pine Island ice-shelf melting to climatic variability. Science 343 (6167), 174–178. https://doi.org/10.1126/science.1244341.

Gao, L., Rintoul, S.R., Yu, W., 2018. Recent wind-driven change in Subantarctic Mode Water and its impact on ocean heat storage. Nat. Clim. Chang. 8 (1), 58–63. https://doi.org/10.1038/s41558-017-0022-8.

Gerringa, L.J., Alderkamp, A.C., Laan, P., Thuroczy, C.E., De Baar, H.J., Mills, M.M., van Dijken, G.L., van Haren, H., Arrigo, K.R., 2012. Iron from melting glaciers fuels the phytoplankton blooms in Amundsen Sea (Southern Ocean): Iron biogeochemistry. Deep-Sea Res. Part II - Top. Stud. Oceanogr. 71, 16–31. https://doi.org/10.1016/j.dsr2.2020.104843.

Gille, S.T., 2008. Decadal-scale temperature trends in the Southern Hemisphere Ocean. J. Clim. 21 (18), 4749–4765. https://doi.org/10.1175/2008JCLI2131.1.

Guo, G., Gao, L., Shi, J., 2021. Modulation of dense shelf water salinity variability in the western Ross Sea associated with the Amundsen Sea Low. Environ. Res. Lett. 16 (1), 014004. https://doi.org/10.1088/1748-9326/abc995.

Ha, H.K., Wåhlin, A.K., Kim, T.W., Lee, S.H., Lee, J.H., Lee, H.J., Hong, C.S., Arneborg, L., Björk, J., Kalén, O., 2014. Circulation and modification of warm deep water on the central Amundsen Shelf. J. Phys. Oceanogr. 44 (5), 1493–1501. https://doi.org/10.1175/JPO-D-13-0240.1.

Hanfland, C., 2002. Radium-226 and Radium-228 in the Atlantic sector of the Southern Ocean. Berichte Zur Polar- Und Meeresforschung 431, 1–135. https://doi.org/10.2312/BzPM_0431_2002.

Hennig, A.N., Mucciarone, D.A., Jacobs, S.S., Mortlock, R.A., Dunbar, R.B., 2024. Meteoric water and glacial melt in the southeastern Amundsen Sea: a time series from 1994 to 2020. Cryosphere 18, 791–818. https://doi.org/10.5194/tc-18-791-2024.

Herraiz-Borreguero, L., Lannuzel, D., van der Merwe, P., Treverrow, A., Pedro, J.B., 2016. Large flux of iron from the Amery Ice Shelf marine ice to Prydz Bay, East Antarctica. J. Geophys. Res. - Oceans 121 (8), 6009–6020. https://doi.org/10.1002/2016JC011687.

Heywood, K.J., Biddle, L.C., Boehme, L., Dutrieux, P., Fedak, M., Jenkins, A., Jones, R. W., Kaiser, J., Mallett, H., Naveira Garabato, A.C., Renfrew, I.A., Stevens, D.P., Webber, B.G., 2016. Between the devil and the deep blue sea: The role of the Amundsen Sea continental shelf in exchanges between ocean and ice shelves. Oceanography 29 (4), 118–129. https://doi.org/10.5670/oceanog.2016.104.

Hohmann, R., Schlosser, P., Jacobs, S., Ludin, A., Weppernig, R., 2002. Excess helium and neon in the southeast Pacific: Tracers for glacial meltwater. J. Geophys. Res. - Oceans 107 (C11), 19. https://doi.org/10.1029/2000JC000378.

Holland, M.M., Landrum, L., Raphael, M.N., Kwok, R., 2018. The regional, seasonal, and lagged influence of the Amundsen Sea Low on Antarctic sea ice. Geophys. Res. Lett. 45 (20), 11–227. https://doi.org/10.1029/2018GL080140.

Jacobs, S.S., Giulivi, C.F., 2010. Large multidecadal salinity trends near the Pacific-Antarctic continental margin. J. Clim. 23 (17), 4508–4524. https://doi.org/10.1175/2010JCLI3284.1.

Jacobs, S.S., Jenkins, A., Giulivi, C.F., Dutrieux, P., 2011. Stronger ocean circulation and increased melting under Pine Island Glacier ice shelf. Nat. Geosci. 4 (8), 519–523. https://doi.org/10.1038/ngeo1188.

Jacobs, S.S., Giulivi, C.F., Dutrieux, P., 2022. Persistent Ross Sea freshening from imbalance west Antarctic ice shelf melting. J. Geophys. Res. - Oceans 127. https://doi.org/10.1029/2021JC017808 e2021JC017808.

Jacobs, S., Jenkins, A., Hellmer, H., Giulivi, C., Nitsche, F., Huber, B., Guerrero, R., 2012. The Amundsen Sea and the Antarctic ice sheet. Oceanography 25 (3), 154–163. https://doi.org/10.5670/oceanog.2012.90.

Jenkins, A., 1999. The impact of melting ice on ocean waters. J. Phys. Oceanogr. 29 (9), 2370–2381. https://doi.org/10.1175/1520-0485(1999)029<2370:TIOMIO>2.0.CO;2.

Jenkins, A., Shoosmith, D., Dutrieux, P., Jacobs, S., Kim, T.W., Lee, S.H., Ha, H.K., Stammerjohn, S., 2018. West Antarctic Ice Sheet retreat in the Amundsen Sea driven by decadal oceanic variability. Nat. Geosci. 11 (10), 733–738. https://doi.org/10.1038/s41561-018-0207-4.

Karstensen, J., Strmma, L., Visbeck, M., 2008. Oxygen minimum zones in the eastern tropical Atlantic and Pacific oceans. Prog. Oceanogr. 77(4), 331 – 350. https://doi: 10.1016/j.pocean.2007.05.009.

Kim, I., Hahm, D., Rhee, T.S., Kim, T.W., Kim, C.S., Lee, S., 2016. The distribution of glacial meltwater in the Amundsen Sea, Antarctica, revealed by dissolved helium and neon. J. Geophys. Res. -Oceans 121 (3), 1654–1666. https://doi.org/10.1002/2015JC011211.

Kim, T.W., Yang, H.W., Dutrieux, P., Wåhlin, A.K., Jenkins, A., Kim, Y.G., Ha, H.K., Kim, C.S., Cho, K.H., Park, T., Park, J., Lee, S.H., Cho, Y.K., 2021. Interannual variaiton of Modified Circumpolar Deep Water in the Dotson-Getz Trough, west Antarctica. J. Geophys. Res. - Oceans 126 (12). https://doi.org/10.1029/2021JC017491 e2021JC017491.

Kipp, L. E., 2018. Radium isotopes as tracers of boundary inputs of nutrients and trace elements to the coastal and open ocean. Doctoral dissertation, Massachusetts

Institute of Technology and Woods Hole Oceanographic Institution, Massachusetts, USA.
Ku, T.L., Lin, M.C., 1976. $^{226}$Ra distribution in the Antarctic Ocean. Earth Planet. Sci. Lett. 32 (2), 236–248.
Ku, T.L., Luo, S., 1994. New appraisal of radium 226 as a large-scale oceanic mixing tracer. J. Geophys. Res. - Oceans 99 (C5), 10255–10273. https://doi.org/10.1029/94JC00089.
Ku, T.L., Li, Y.H., Mathieu, G.G., Wong, H.K., 1970. Radium in the Indian-Antarctic Ocean south of Australia. J. Geophys. Res. - Oceans 75 (27), 5286–5292.
Li, Q., Chen, M., Jia, R., Zeng, J., Lin, H., Zheng, M., Qiu, Y., 2017. Transit time of river water in the Bering and Chukchi Seas estimated from $\delta^{18}$O and radium isotopes. Prog. Oceanogr. 159, 115–129. https://doi.org/10.1016/j.pocean.2017.08.004.
Loose, B., Jenkins, W.J., 2014. The five stable noble gases are sensitive unambiguous tracers of glacial meltwater. Geophys. Res. Lett. 41 (8), 2835–2841. https://doi.org/10.1002/2013GL058804.
Macdonald, R.W., Paton, D.W., Carmack, E.C., Omstedt, A., 1995. The freshwater budget and under-ice spreading of Mackenzie River water in the Canadian Beaufort Sea based on salinity and $^{18}$O/$^{16}$O measurements in water and ice. J. Geophys. Res.-Oceans 100 (C1), 895–919. https://doi.org/10.1029/94JC02700.
Martinson, D.G., 2012. Antarctic circumpolar current's role in the Antarctic ice system: An overview. Paleogeogr. Paleoclimatol. Paleoecol. 335, 71–74. https://doi.org/10.1016/j.palaeo.2011.04.007.
Meredith, M.P., Brandon, M.A., Wallace, M.I., Clarke, A., Leng, M.J., Renfrew, I.A., van Lipzig, N.P., King, J.C., 2008. Variability in the freshwater balance of northern Marguerite Bay, Antarctic Peninsula: results from $\delta^{18}$O. Deep-Sea Res. Part II - Top. Stud. Oceanogr. 55 (3–4), 309–322. https://doi.org/10.1016/j.dsr2.2007.11.005.
Meredith, M.P., Wallace, M.I., Stammerjohn, S.E., Renfrew, I.A., Clarke, A., Venables, H. J., Shoosmith, D.R., Souster, T., Leng, M.J., 2010. Changes in the freshwater composition of the upper ocean west of the Antarctic Peninsula during the first decade of the 21st century. Prog. Oceanogr. 87 (1–4), 127–143. https://doi.org/10.1016/j.pocean.2010.09.019.
Meredith, M.P., Venables, H.J., Clarke, A., Ducklow, H.W., Erickson, M., Leng, M.J., Lenaerts, J.T., van den Broeke, M.R., 2013. The freshwater system west of the Antarctic Peninsula: spatial and temporal changes. J. Clim. 26 (5), 1669–1684. https://doi.org/10.1175/JCLI-D-12-00246.1.
Moore, W.S., 1987. Radium 228 in the South Atlantic Bight. J. Geophys. Res. -Oceans 92 (C5), 5177–5190. https://doi.org/10.1029/JC092iC05p05177.
Moore, W.S., 1998. Application of $^{226}$Ra, $^{228}$Ra, $^{223}$Ra, and $^{224}$Ra in coastal waters to assessing coastal mixing rates and groundwater discharge to oceans. J. Earth Syst. Sci. 107 (4), 343–349. https://doi.org/10.1007/BF02841600.
Östlund, H.G., Hut, G., 1984. Arctic Ocean water mass balance from isotope data. J. Geophys. Res. - Oceans 89 (C4), 6373–6381. https://doi.org/10.1029/JC089iC04p06373.
Paolo, F.S., Fricker, H.A., Padman, L., 2015. Volume loss from Antarctic ice shelves is accelerating. Science 348 (6232), 327–331. https://doi.org/10.1126/science.aaa0940.
Pritchard, H., Ligtenberg, S.R., Fricker, H.A., Vaughan, D.G., van den Broeke, M.R., Padman, L., 2012. Antarctic ice-sheet loss driven by basal melting of ice shelves. Nature 484 (7395), 502–505. https://doi.org/10.1038/nature10968.
Randall-Goodwin, E., Meredith, M.P., Jenkins, A., Yager, P.L., Sherrell, R.M., Abrahamsen, E.P., Guerrero, R., Yuan, X., Mortlock, R.A., Gavahan, K., Alderkamp, A.C., Ducklow, H., Robertson, R., Carmack, E.C., 2015. Freshwater distributions and water mass structure in the Amundsen Sea Polynya region Antarctica. Elementa - Sci. Anthrop. 3, 000065. https://doi.org/10.12952/journal.elementa.000065.
Rignot, E., Jacobs, S.S., 2002. Rapid bottom melting widespread near Antarctic ice sheet grounding lines. Science 296 (5575), 2020–2023. https://doi.org/10.1126/science.1070942.
Rignot, E., Jacobs, S., Mouginot, J., Scheuchl, B., 2013. Ice-shelf melting around Antarctica. Science 341 (6143), 266–270. https://doi.org/10.1126/science.1235798.
Scheuchl, B., Mouginot, J., Rignot, E., Morlighem, M., Khazendar, A., 2016. Grounding line retreat of Pope, Smith, and Kohler Glaciers, West Antarctica, measured with Sentinel-1a radar interferometry data. Geophys. Res. Lett. 43 (16), 8572–8579. https://doi.org/10.1002/2016GL069287.
Schlitzer, R., 2018. Ocean data view. http://odv.awi.de.
Schmidtko, S., Heywood, K.J., Thompson, A.F., Aoki, S., 2014. Multidecadal warming of Antarctic waters. Science 346 (6214), 1227–1231. https://doi.org/10.1126/science.1256117.
Sherrell, R.M., Lagerström, M.E., Forsch, K.O., Stammerjohn, S.E., Yager, P.L., 2015. Dynamics of dissolved iron and other bioactive trace metals (Mn, Ni, Cu, Zn) in the Amundsen Sea Polynya Antarctica. Elementa - Sci. Anthrop. 3, 000071. https://doi.org/10.12952/journal.elementa.000071.
Silvano, A., Rintoul, S.R., Peña-Molino, B., Hobbs, W.R., van Wijk, E., Aoki, S., Tamura, T., Williams, G.D., 2018. Freshening by glacial meltwater enhances melting of ice shelves and reduces formation of Antarctic Bottom Water. Sci. Adv. 4 (4), eaap9467. https://doi.org/10.1126/sciadv.aap9467.
Skrzypek, G., Ford, D., 2014. Stable isotope analysis of saline water samples on a cavity ring-down spectroscopy instrument. Environ. Sci. Technol. 48 (5), 2827–2834. https://doi.org/10.1021/es4049412.
Stanley, R.H., Jenkins, W.J., Lott III, D.E., Doney, S.C., 2009. Noble gas constraints on air-sea gas exchange and bubble fluxes. J. Geophys. Res. - Oceans 114, C11020. https://doi.org/10.1029/2009JC005396.
St-Laurent, P., Klinck, J.M., Dimmiman, M.S., 2015. Impact of local winter cooling on the melt of Pine Island Glacier. Antarctica. J. Geophys. Res. – Oceans 120, 6718–6732. https://doi.org/10.1002/2015JC010709.
St-Laurent, P., Yager, P.L., Sherrell, R.M., Stammerjohn, S.E., Dinniman, M.S., 2017. Pathways and supply of dissolved iron in the Amundsen Sea (Antarctica). J. Geophys. Res. - Oceans 122 (9), 7135–7162. https://doi.org/10.1002/2017JC013162.
The IMBIE team, 2018. Mass balance of the Antarctic Ice Sheet from 1992 to 2017. Nature 558, 219 - 222. DOI: 10.1038/s41586-018-0179-y.
Thomas, E.R., Dennis, P.F., Bracegirdle, T.J., Franzke, C., 2009. Ice core evidence for significant 100-year regional warming on the Antarctic Peninsula. Geophys. Res. Lett. 36 (20). https://doi.org/10.1029/2009GL040104.
Turner, J., Phillips, T., Hosking, J.S., Marshall, G.J., Orr, A., 2013. The Amundsen Sea Low. Int. J. Climatol. 33 (7), 1818–1829. https://doi.org/10.1002/joc.3558.
Vernet, M., Smith Jr, K.L., Cefarelli, A.O., Helly, J.J., Kaufmann, R.S., Lin, H., Long, D.G., Murray, A.E., Robison, B.H., Ruhl, H.A., Shaw, T.J., Sherman, A.D., Sprintall, J., Stephenson Jr, G.R., Stuart, K.M., Twining, B.S., 2012. Islands of ice: Influence of free-drifting Antarctic icebergs on pelagic marine ecosystems. Oceanography 25 (3), 38–39. https://doi.org/10.5670/oceanog.2012.72.
Wåhlin, A.K., Yuan, X., Björk, G., Nohr, C., 2010. Inflow of warm Circumpolar Deep Water in the central Amundsen shelf. J. Phys. Oceanogr. 40 (6), 1427–1434. https://doi.org/10.1175/2010JPO4431.1.
Walker, D.P., Brandon, M.A., Jenkins, A., Allen, J.T., Dowdeswell, J.A., Evans, J., 2007. Oceanic heat transport onto the Amundsen Sea shelf through a submarine glacial trough. Geophys. Res. Lett. 34 (2), L02602. https://doi.org/10.1029/2006GL028154.
Wang, B., Chen, M., Chen, F., Jia, R., Li, X., Zheng, M., Qiu, Y., 2020. Meteoric water promotes phytoplankton carbon fixation and iron uptake off the eastern tip of the Antarctic Peninsula (eAP). Prog. Oceanogr. 185, 101347. https://doi.org/10.1016/j.pocean.2020.102347.
Webber, B.G., Heywood, K.J., Stevens, D.P., Dutrieux, P., Abrahamsen, E.P., Jenkins, A., Jacobs, S.S., Ha, H.K., Lee, S.H., Kim, T.W., 2017. Mechanisms driving variability in the ocean forcing of Pine Island Glacier. Nat. Commun. 8 (1), 1–8. https://doi.org/10.1038/ncomms14507.
Williams, G.D., Herraiz-Borreguero, L., Roquet, F., Tamura, T., Ohshima, K.I., Fukamachi, Y., Fraser, A.D., Gao, L., Chen, H., McMahon, C.R., Harcourt, R., Hindell, M., 2016. The suppression of Antarctic bottom water formation by melting ice shelves in Prydz Bay. Nat. Commun. 7 (1), 1–9. https://doi.org/10.1038/ncomms12577.
Xie, Y., Huang, Y., Shi, W., Qiu, Y., 1994. Simultaneous concentration and determination of $^{226}$Ra, $^{228}$Ra in natural waters. J. Xiamen Univ. (nat. Sci.) 33 (Sup.), 86–90 in Chinese, with English summary.
Yager, P.L., Sherrell, R.M., Stammerjohn, S.E., Alderkamp, A.-C., Schofield, O., Abrahamsen, E.P., Arrigo, K.R., Bertilsson, S., Garay, D.L., Guerrero, R., Lowry, K.E., Moksnes, P.-O., Ndungu, K., Post, A.F., Randall-Goodwin, E., Riemann, L., Severmann, S., Thatje, S., van Dijken, G.L., Wilson, S., 2012. ASPIRE: The Amundsen Sea Polynya International Research Expedition. Oceanography 25 (3), 40–53. https://doi.org/10.5670/oceanog.2012.73.
Yang, H.W., Kim, T.W., Dutrieux, P., Wåhlin, A.K., Jenkins, A., Ha, H.K., Kim, C.S., Cho, K.H., Park, T., Lee, S.H., Cho, Y.K., 2022. Seasonal variability of ocean circulation near the Dotson Ice Shelf Antarctica. Nat. Commun. 13, 1138. https://doi.org/10.1038/s41467-022-28751-5.
Zheng, M., Chen, M., Yang, J., Zhang, R., Ma, Q., Yang, W., Qiu, Y., 2010. Radium-226 as a tracer for the source and movement of water masses in the Prydz Bay of Antarctica. Acta Oceanol. Sin. 32 (4), 88–97 in Chinese, with English Abstract.
Zheng, Y., Heywood, K.J., Webber, B.G., Stevens, D.P., Biddle, L.C., Boehme, L., Loose, B., 2021. Winter seal-based observations reveal glacial meltwater surfacing in the southeastern Amundsen Sea. Commun. Earth Environm. 2, 40. https://doi.org/10.1038/s43247-021-00111-z.